



Optimization of friction stir welding for various tool pin geometries: the weldability of Polyamide 6 plates made of material extrusion additive manufacturing

Nectarios Vidakis¹ · Markos Petousis¹ · Nikolaos Mountakis¹ · John D. Kechagias²

Received: 14 September 2022 / Accepted: 6 December 2022 / Published online: 20 December 2022
© The Author(s), under exclusive licence to Springer-Verlag London Ltd., part of Springer Nature 2022

Abstract

The weldability of 3D printed (3DP), through material extrusion (MEX), of Polyamide 6 (PA6) plates joined with FSW is investigated. FSW has its challenges in polymers, especially for 3D printed parts, while it is used for various industrial applications in the automotive and aerospace sector, in joints, and in other types of parts. Herein, a full factorial experimental course was deployed, to quantitatively document the impact of three critical process parameters (e.g., the rotational speed and the travel speed of the tool, as well as the pin geometry of the tool) and to optimize their levels. A set of identical PA6 prismatic workpieces was prepared and then welded. Throughout the welding process, the temperature profiles were monitored and logged, to ensure the solid state of the workpiece material. The welding efficiency of the joints was then determined through mechanical tests, while unwelded 3D printed specimens were employed as control samples. Thorough morphological evaluations and characterization with microscopy (Scanning Electron and optical Microscopy) were performed for the welding zones. The evaluation of the metrics with statistical modeling tools led to the quantitative correlation of the process parameters, as well as their interactions, and finally optimization. The feasibility of joining 3DP PA6 with FSW was verified, reaching a welding efficiency of up to 120.40% for threaded cylindrical pin profile, rotational speed 1200 rpm, and travel speed 3 mm/min. The results of the study provide valuable information and merit for the FSW of 3DP PA6, which can be exploited in various industrial applications.

Keywords Friction stir welding (FSW) · Polyamide 6 (PA6) · Material extrusion (MEX) · Hybrid additive manufacturing · Optimization

Abbreviations

3DP	3D printing	BT	Bed temperature
ABS	Acrylonitrile butadiene styrene	CAGR	Compound annual growth rate
AM	Additive manufacturing	CCW	Counterclockwise
ANN	Artificial neural networks	CHT	Chamber heat temperature
ANOVA	Analysis of variances	CNC	Computer numeric control
AS	Advancing side	CW	Clockwise
		DOE	Design of experiment
		DSC	Differential scanning calorimetry
		E	Tensile modulus of elasticity
		FDM	Fused filament fabrication
		FEA	Finite elements analysis
		FFF	Fused filament fabrication
		FSW	Friction stir welding
		HAZ	Heat-affected zone
		HAM	Hybrid additive manufacturing
		HDPE	High-density polyethylene
		MAPE	Mean absolute percentage error
		MCU	Machine control unit
		MEP	Main effect plot

✉ Markos Petousis
markospetousis@hmu.gr

Nectarios Vidakis
vidakis@hmu.gr

Nikolaos Mountakis
mountakis@hmu.gr

John D. Kechagias
jkechag@uth.gr

¹ Hellenic Mediterranean University, 71410 Heraklion, Greece

² University of Thessaly, 43100 Karditsa, Greece

MEX	Material extrusion
MFI	Melt flow index
NN	Neural network
NT	Nozzle temperature
NZ	Nugget zone
OA	Orthogonal array
PA	Polyamide
PLA	Polylactic acid
PET-G	Polyethylene terephthalate glycol
PP	Polypropylene
PPA	Pin profile A (cylindrical)
PPB	Pin profile B (frustum)
PPC	Pin profile C (threaded cylindrical)
PPD	Pin profile D (threaded frustum)
PS	Print speed
Ra	Average surface roughness: average profile height deviations from the mean line
RDA	Raster deposition angle
Rz	Surface roughness: min–max peak to valley height of the profile, within five sampling lengths
RS	Rotational speed
RT	Residual thickness
RTS	Retreating side
RPM	Revolutions per minute
sB	Tensile strength
SEM	Scanning electron microscopy
SCRM	Separated cubic regression model
SSP	Stair stepping phenomenon
SV	Side view
Tg	Glass transition temperature
TGA	Thermogravimetric analysis
TMZ	Thermomechanically affected zone
TPU	Thermoplastic polyurethane
TS	Travel speed
TV	Top view
WE	Weld efficiency
WT	Welding temperature

1 Introduction

Polyamide 6 (PA6) is a widely adopted and popular polymeric matrix, used in several types of industries and applications, such as marine applications [1], electrical applications, buildings, and engineering products [2]. Consequently, massive research has been conducted on various aspects of the polymer's performance. Arhant et al. [1] searched the mechanical, thermal, and economic performance of the PA6 polymer, to investigate the potential of using it in pressure vessels operating at 4500 m deep-sea waters. Jimenez et al. [2] investigated its resistance to flames, for potential electrical applications. The effect of reprocessing the PA6 upon the

mechanical response of the polymeric matrix, to investigate its potential for sustainable, circular economy applications has also been investigated [3]. The chemical, molecular, rheological, and crystalline behavior has also been investigated for up to 16 reprocessing cycles [4]. PA6 has been used as a matrix material, aiming to enhance its mechanical properties, with the addition of silicon carbide for composite gear manufacturing for the automotive industry [5]. The potential of composites with short carbon fibers as reinforcement was investigated, for the enhancement of mechanical and thermomechanical performance [6]. The enhancement of both the mechanical and electrical properties of the PA6 polymer was investigated by using carbon nanotubes for antistatic packaging [7] and blends with acrylonitrile butadiene styrene (ABS) [8].

Due to its popularity, it has been used and investigated in various Additive Manufacturing (AM) technologies. In material extrusion (MEX) 3D Printing (3DP), Jia et al. [9] developed a PA6 filament, with improved processability performance to facilitate the process. Polyamide's MEX 3DP parameters have been processed with statistical modeling tools, to achieve optimal mechanical performance [10]. The effect of strain rate on its mechanical response, when loading 3DP PA6 with tensile loads, showed that the polymer robustness is not significantly affected by the loading rate [11]. At the same time, it can withstand up to six recycling processes, without compromising its mechanical strength [12]. Its mechanical and tribological properties have also been investigated in powder bed fusion 3DP and enhanced with composites development [13]. The performance of the polyamides in powder bed fusion 3DP and material jetting 3DP has been compared, showing insignificant differences in the mechanical response, but significant differences in the surface quality and the smoothness of the parts, which each process is superior to the other in different areas [14].

Friction Stir Welding (FSW) is a procedure for joining materials, presented by the British Welding Institute (TWI) in 1991. Initially, the process was developed for metallic matrices with limited weldability through fusion processes [15]. Its popularity as a joining process is attributed to its characteristics. It is an autogenous process, with a non-consumable welding tool, that does not require special gases to be performed, and consumes less energy than most welding processes [16]. It was initially applied in aluminum, which is thoroughly studied in the process [16–23]. As expected, the effect of the FSW parameters, such as the weld tool geometry, the tool speed, and the rotational speed, among others, on the joint performance for different Al grades is a popular subject in the literature [24–31], and although several works have been presented, there are still areas that need further study. For aluminum, more advanced research has been presented for the AA6061 grade, related to numerical analysis [32, 33], the vibration effects [34, 35], the dynamic

recrystallization phenomenon [36], and the thermal treatment and wear behavior [37]. Additionally, the introduction of nanoparticles such as silicon carbide, as reinforcement, in aluminum alloys (grade AA6061) in FSW has been investigated [38–40]. FSW of aluminum parts has been applied in various industries [41], such as in the automobile sector, marine applications, railways, and aerospace industries [42].

As expected, research has expanded in thermoplastics, due to their wide use in parts and the feasibility and the performance of the process, and its parameters have been thoroughly investigated [43]. FSW in polymers is applied in different engineering fields [43, 44], such as in joints [45]. Research is focusing on different aspects of the process, aiming to improve its performance, considering the characteristics of the thermoplastics. Towards this direction, Banjare et al. [46] presented a heating tool specially designed to improve the performance of the weld when joining thermoplastics with the FSW process. Singh et al. [47] highlighted the need for studying the feasibility of joining 3D-printed thermoplastic parts since the research so far indicated differences in the response of bulk and 3D-printed thermoplastics in FSW. Therefore, in this study, the current trends, and the optimization of the mechanical strength of 3D-built thermoplastics welded with FSW are presented. Kumar et al. investigated the feasibility of joining 3D-printed PLA/Al composites with a semi-consumable weld tool. The effect of the FSW parameters on the weld performance was considered [48]. Sheikh-Ahmad et al. [49] also studied the performance of composites in the FSW process. They investigated high-density polyethylene (HDPE)/Carbon black (CB) composites, focusing on the effect of temperature on the process performance. Lambiase et al. [50] also investigated the developed temperature (and loads) with various weld tool rotational speeds on polycarbonate (PC) samples. Tiwary et al. [51] investigated the joining with FSW of dissimilar PLA/ABS sheets. Nylon micro-particles were introduced to enhance the mechanical strength of the weld, for direct use in the process in UAVs. It was found that the addition of the Nylon particles had a different effect on the PLA and the ABS. When joining dissimilar (ABS and PA6) 3D printed sheets with FSW [52], it was found that the weld is very weak, due to the different melt flow index of the two polymers. Reinforcement with Al was used to achieve a similar MFI and as a result an acceptable joint.

In HAM, various post-processing manufacturing procedures have been applied and investigated for the 3D-printed parts [53]. For the FSW of 3D printed sheets studies have been presented for the ABS [54], PLA [55], and Poly(methyl methacrylate) (PMMA) [56]. These works dealt with the impact of critical FSW factors on the joint's performance (welding efficiency of the welded parts). Statistical modeling tools were used to optimize the process. The feasibility of joining composite structures, using ABS as the matrix

material, has also been investigated [57]. Bagheri et al. [58] studied the fatigue strength of parts joined with rotary Friction Welding (FW), not FSW. Bulk ABS was welded with 3D-printed ABS and PLA samples.

Polyamides research is focusing on the study of the set parameters and their influence on the mechanical efficiency of the joints, using statistical modeling tools [59, 60]. Both studies employ ANOVA to optimize the tensile strength of PA66 plates, by studying parameters, such as the tool rotational speed and the feed rate. Nandhini et al. [61] studied additionally the impact of the tool plunge on the joint's hardness and the temperature developed during the process [62]. Zafar et al. examined the effect of the FSW parameters on the flow and the thermal response of thick PA6 plates. They reported the differences in the behavior of the material, they found between the FSW of metals and PA6 [63]. The FSW of PA6 has also been modeled with Finite Elements Analysis (FEA) and the strain distribution and the flow mechanics concerning the temperature were successfully estimated. The model has been experimentally verified [64]. Zinati et al. [65] experimentally studied the feasibility of joining PA6 with PA6/MWCNTs composites with the friction stir process. Numerical modeling was developed, employing the Lagrangian incremental formulation and the outcomes were claimed to be compliant with the experimental findings. Yan et al. [66] inspected the effect of various parameters on the morphology and the mechanical performance when joining dissimilar Aluminum AA6061 alloys with glass fiber reinforced PA6, with a friction lap welding process. They are reporting that the mechanical performance of the joint is increased, with the increase of the grooves.

Research on the feasibility of joining 3DP PA sheets is still very limited. Joining with FSW of dissimilar Al composites thermoplastics (ABS with PA6) has been investigated for mechanical strength and their rheological properties [67] and a semi-consumable welding tool [52]. Singh et al. have studied the mechanical and morphological properties when joining MEX 3DP dissimilar Al composites thermoplastics (ABS with PA6) in cylindrical disks form, with Friction Welding (FW), not FSW, on a lathe machine [68]. To the authors' best knowledge, there is not yet any research offered in the corresponding literature, dealing with the probability of joining MEX 3DP PA6 and the effect of the FSW parameters on the performance of the joints. The feasibility of joining 3DP parts with FSW and their performance needs to be studied, due to their heterogeneous nature, their porosity, and their structure, which can affect the process. For this reason, results in the literature for bulk, injection-molded PA6 sheets cannot be assumed reliable for the corresponding 3DP parts.

This work investigates the process of joining with FSW MEX 3DP PA6 plates. The feasibility and the performance of the produced weld, which is affected by both the 3DP and

the FSW process, are studied and reported, in this hybrid additive manufacturing (HAM) procedure. Being able to join 3DP parts exploits the benefits of 3DP and expands its field of applications, in areas, such as large parts construction, and repairing of parts, among other. Tiwary et al. [69] highlighted the limitations of the 3D printed parts' size, which could be overcome with the FSW process, for the formation of larger size parts, for the biomedical, aerospace, and automotive field. Welding 3D polymeric parts together have enormous potential since it allows the production of parts, that, due to their geometry or other characteristics, cannot be produced using standard manufacturing techniques. Additionally, large-scale components that are too large to be manufactured using 3D printing and polymeric materials can be bonded using FSW after being 3D printed.

FSW of polymers has its challenges and is a rather new subject in the literature, not thoroughly studied yet, according to the literature review. The effect of the 3D printing structure of the polymeric parts is also an additional challenge in the FSW process, with the number of published works in the area being very limited. The novelty of the work is that it covers this gap in the research, by providing reliable experimental results and analysis with statistical modeling tools, about the feasibility of the process and the performance of PA6 3D printed sheets when joined with the FSW process. The process is optimized, and the control parameter values that provide the optimal results are indicated. No similar research exists in the literature so far, according to the authors' best knowledge, on the FSW of MEX 3D printed PA6 parts. The comprehension of the behavior and the performance of PA6 MEX 3D printed sheets when joined with the FSW process can be exploited also for the joining of 3D printed parts with injection molding parts of the same or some other polymer. Joining dissimilar polymers is also a subject investigated in the literature, according to the presented literature review, but not for the PA6 in 3D printing. Such types of applications further expand the merit of the results of the work. This is now discussed in the revised version of the manuscript.

The challenges of joining MEX 3D printed polymers can be attributed to the built-in porosity, anisotropy, and built-in structural structure of 3D printed parts. As a result welding, them can be a difficult procedure. Here, this was accomplished for the first time for the PA6 polymer 3D printed with the MEX process. An initial assessment of the impact of the FSW parameters was made. 3DP parts were prepared and welded with different FSW parameters. The contribution of specific FSW parameters (welding speed, welding tool rotational speed, weld tool geometry) was investigated, and the experimental findings were analyzed in depth with statistical and modeling tools. Analytical and numerical models have been presented in the literature for the FSW of polymeric parts (PMMA and Polycarbonate – PC sheets,

[45, 70]). These models advance existing models for metallic alloys, and they operate under the principle that the materials behave in a bulky and isotropic way. This assumption is reasonable for metallic alloys and satisfactory for bulk polymers. MEX 3D printed parts, due to their internal structure, are not homogenous and isotropic. These characteristics are presented in a stochastic manner, depending on the 3D printing parameters. Additionally, in contrast to other fabrication procedures, the porosity (voids are formed also for full infill density), the increased roughness of the produced surfaces, and the dimensional deviations remain inevitable. Therefore, using the aforementioned numerical and/or analytical thermomechanical simulations will not yield accurate or generally acceptable outcomes. Even the variances in commercial filament quality cause noticeable differences between studies using filaments made from the same materials but sold by other suppliers.

In this work, the filament for the 3D printing of the samples was manufactured within the contents of the study, by using raw materials with known technical characteristics. All the thermomechanical experiments (TGA, DSC, etc.) were conducted in the material, to ensure the credibility of these properties since differences are expected when using such data from other research groups for nominally the same material but with different specifications or grades. The experimental findings in the work verified the stochastic nature of the parameters' measurements, verifying the need and the importance of the statistical analysis implemented within the work. At the same time, it was evident that quasi-static analysis or numerical modeling are not adequate approaches for 3D printed parts. During the experimental procedure, the temperature was monitored, to confirm that the FSW experiments were performed with the joined materials being in solid-state, as the FSW procedure instructs, and no melting occurred. Additionally, the temperature was correlated along with the mechanical properties and the measured minimum Residual Thickness of the samples with the control parameters investigated herein (weld tool geometry, weld, and rotational speed). For the evaluation of the weld performance, welded specimens were tested in tensile tests. Their morphological characteristics were also examined with optical and Scanning Electron Microscopy. The weld tool geometry was proved to have a weighty impact on the strength of the joints, although all the parameters studied have an impact on the weld result.

2 Materials and methods

The main experimental and methodological steps followed in the current work, for the 3DP preparation of the specimens, the FSW course, and the evaluation of the joints'

performance, are highlighted in Fig. 1 and are described in detail further below.

2.1 FSW experiments

For the preparation of the MEX 3DP specimens, Novamid NX 160 PA6 (density 1140 kg/m^3 , melting temperature $193 \text{ }^\circ\text{C}$) pellets were extruded to the filament in a 3devo Composer single screw extruder ($190 \text{ }^\circ\text{C}$ at the outer heating zones, and $220 \text{ }^\circ\text{C}$ at the middle heating zones, 3.5 rpm screw rotational speed). The filament was then utilized for the MEX 3DP of the specimens. Regarding the MEX-3D printing conditions, the applied settings were thoroughly optimized through the former experimental works of the authors [10, 71] and are presented in Fig. 2. The filament was then 3D-Printed to produce workpieces to be welded, suitable for the fixture prepared for the Computer Numeric Control (CNC) milling machine, with the aid of an Intamsys Funmat HT 3D Printing Device (Intamsys Technology Co. Ltd., Shanghai, China).

The 3DP specimens' thermal properties were depicted through Thermogravimetric analysis (TGA), as well as

through Differential Scanning Calorimetry (DSC). Herby, the solid-state of the Polyamide 6 throughout the welding course is able to be ensured. TGA measurements were taken on a Perkin Elmer Diamond device with the following thermal scheme: heating $30\text{--}550 \text{ }^\circ\text{C}$, increase $10 \text{ }^\circ\text{C/min}$. DSC was conducted in a TA Instruments DSC 25 device, with the following thermal scheme 25 up to 220 down to $25 \text{ }^\circ\text{C}$, heating rate $15 \text{ }^\circ\text{C/min}$.

Weld specimens' dimensions and building strategy are presented in Fig. 2. Two such specimens were welded along a common edge on their long side for each repetition of the process on a Haas TM-1P CNC milling machine (the machine's MCU was used for the G-code programming). Twelve tensile specimens are produced, i.e., three sets of four specimens each (with 10 mm width each), welded with different FSW parameters in each set of the four specimens. The weld tool rotational speed and the welding speed changed at specific lengths to produce the different specimens, according to the aforementioned scenario. The weld tool was the same in each such set. These sets were repeated with four different weld tools geometries, presented in Fig. 2. Weld tools were fabricated on a Haas SL20 lathe

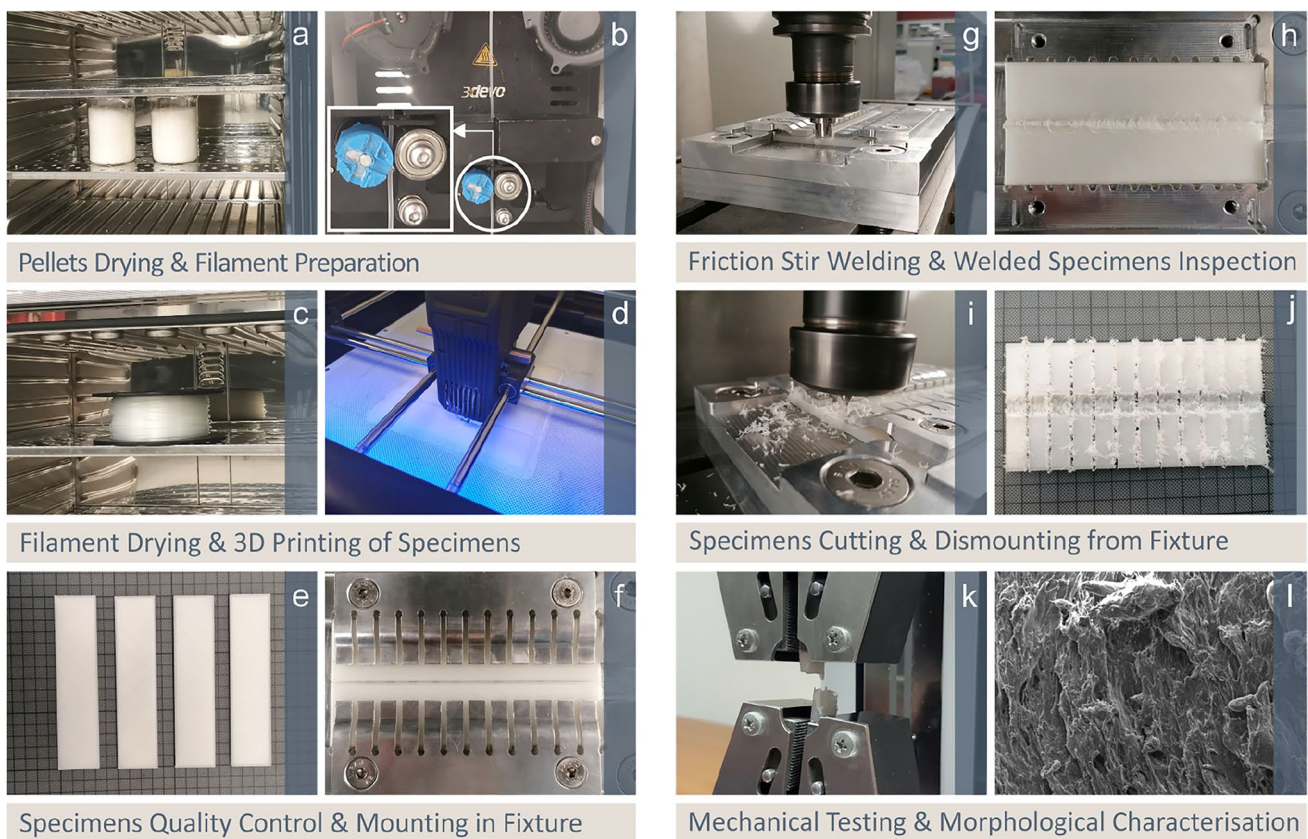


Fig. 1 (a) Pellets oven drying, (b) filament melt extrusion, (c) filament oven drying, (d) 3D fabrication of workpieces, (e) 3DP specimens, (f) fixing of the weld specimens in the Computer Numeric Control (CNC) milling machine, (g) FSW of the specimens, (h) the

completed welded part, (i) cutting of the part into tensile test specimens, (j) the milled cut tensile test specimens, (k) tensile tests of the welded probes, (l) optical and SEM morphological characterization of the specimens

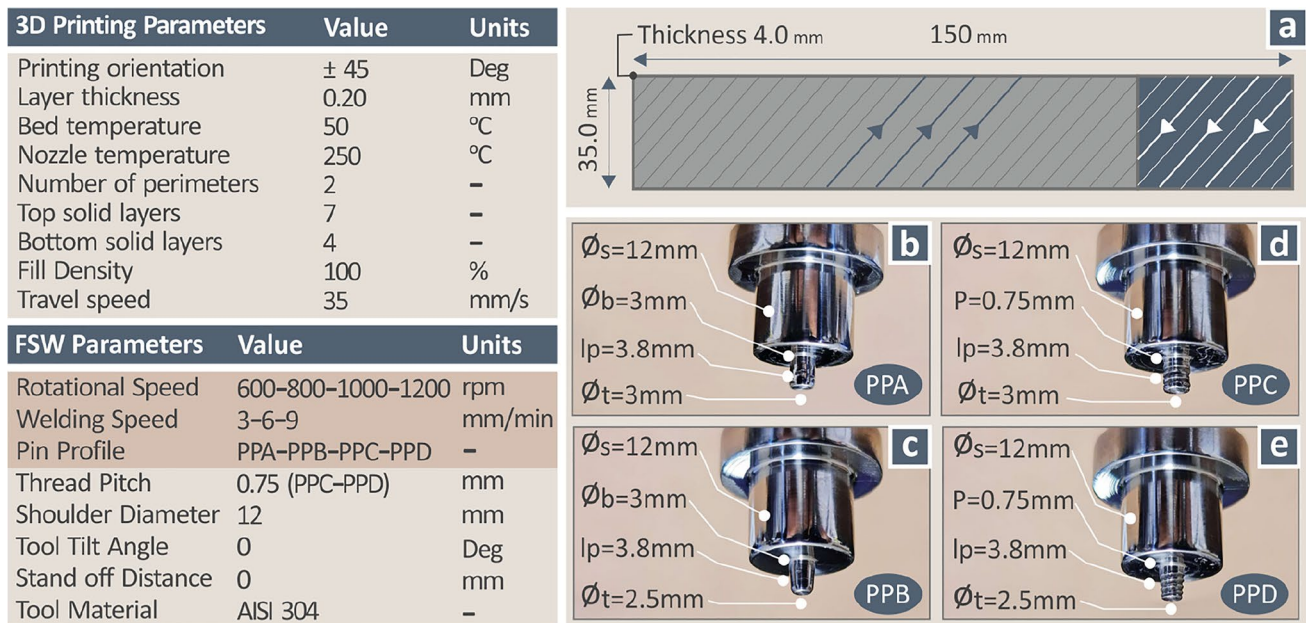


Fig. 2 MEX 3DP and FSW process parameters of this work and (a) weld specimen geometry and 3DP build structure, and geometry of the welding tools studied (b) PPA, (c) PPB, (d) PPC, (e) PPD

using AISI304L stainless steel bars. The weld-tools surfaces were polished after the completion of the fabrication process. Weld tools were differentiated in their pin geometry, to evaluate their effect on the process. Profile Pin A (PPA) tool had a cylindrical pin (Fig. 2b), and a PPB frustum pin (Fig. 2c), while PPC (Fig. 2d) and PPD (Fig. 2e) have the corresponding pin geometries with 0.75 mm pitch thread.

A Flir One Pro thermal imaging camera was monitoring the specimens' temperature during the welding process, to document the thermal course and the material state, throughout the joining process. The welded specimen is automatically cut into these specimens (by replacing the welding tool with a proper milling tool), after the completion of the welding process in the CNC milling machine.

2.2 Design of experiments

The process optimization in this study utilizes a full factorial experimental array that each combination repeated three times (see Table 1). So, four levels were decided for the rotational speed (RS; 600, 800, 1000, 1200 rpm), and three levels for the travel speed (TS; 3, 6, 9 mm/min) which were applied in four different tools (PP—A—B—C—D; see Fig. 2). The total experimental effort reaches 144 discrete experiments, a large amount to optimize the process with confidence [72]. In each experiment, the output was the RT, WT, sB, and E. Regarding the range of the FSW parameters, the authors paid special attention to ensuring the solid-state status of the process. Moreover, exhaustive screening FSW experiments have been performed, in order to reach satisfactory

weldability, to ensure a maximum acceptable decrease of the joints' thickness, and to obtain clear and stable seams. The parameter's range of the full factorial analysis has been reached through such screening tests. A critical review of the literature related to the FSW process on polymers was made, in order to document and delimit the range of the control parameters in these screening tests.

2.3 Weld performance evaluation

For the evaluation of the weld performance, welded specimens were subjected to tensile tests, by means of an Imada MX2 test device (at the strain rate of 10 mm/min). Non-welded samples were also fabricated and tested as control samples. The samples' morphological characteristics around the weld region (NZ, TMZ, HAZ) were also assessed with optical microscopy (Kern OKO 1), stereoscopy (KERN OZR5), employing a KERN ODC 832 camera (5MP), and Scanning Electron Microscopy (SEM) microscope (JEOL JSM 6362LV, gold-sputtered samples, 20 kV).

3 Results

3.1 FSW experimentation and results valuation

The FSW procedure carried out in this work is illustrated in Fig. 3. This is a two-step process. First, the weld specimens are joined with FSW (Fig. 3a), and then the weld part is cut into three groups of tensile specimens of four specimens

Table 1 Full factorial design: control parameters and levels

Run	Tool	RS	TS
1	PPA	600	3
2	PPA	600	6
3	PPA	600	9
4	PPA	800	3
5	PPA	800	6
6	PPA	800	9
7	PPA	1000	3
8	PPA	1000	6
9	PPA	1000	9
10	PPA	1200	3
11	PPA	1200	6
12	PPA	1200	9
13	PPB	600	3
14	PPB	600	6
15	PPB	600	9
16	PPB	800	3
17	PPB	800	6
18	PPB	800	9
19	PPB	1000	3
20	PPB	1000	6
21	PPB	1000	9
22	PPB	1200	3
23	PPB	1200	6
24	PPB	1200	9
25	PPC	600	3
26	PPC	600	6
27	PPC	600	9
28	PPC	800	3
29	PPC	800	6
30	PPC	800	9
31	PPC	1000	3
32	PPC	1000	6
33	PPC	1000	9
34	PPC	1200	3
35	PPC	1200	6
36	PPC	1200	9
37	PPD	600	3
38	PPD	600	6
39	PPD	600	9
40	PPD	800	3
41	PPD	800	6
42	PPD	800	9
43	PPD	1000	3
44	PPD	1000	6
45	PPD	1000	9
46	PPD	1200	3
47	PPD	1200	6
48	PPD	1200	9

each (Fig. 3b). Each group of specimens is welded with different FSW parameters (Fig. 3c). The temperature developed during the process is monitored and, in this case, it is shown that the increase in the travel speed (TS), leads to a slight reduction in the maximum temperature. It should be mentioned that the tool starts from outside the seam and enters the weld seam from the side (does not lower on the top of the seam), where it stays in the transient region for an adequate amount of time, to increase the temperature of the tool and the specimens to an acceptable level at the beginning of the process. As the weld tool moves during the FSW process, small parts (debris) of the typical superficial strands of the 3D printing texture of the samples are not welded, they brake and are scattered on the top surface of the samples (Fig. 3b).

The produced weld seams with the four different weld tools studied in this work are presented in Fig. 4 (Fig. 4a – PPA tool, Fig. 4c PPB tool, Fig. 4e PPC tool, Fig. 4g PPD tool). Next to each weld seam, corresponding tensile stress vs. strain graphs are presented (Fig. 4b – PPA tool, Fig. 4b PPB tool, Fig. 4f PPC tool, Fig. 4h PPD tool), for the different Travel Speeds (TS) of this work. All stress–strain cases within the figure are for specimens welded at 800 rpm rotational speed (RS). In all graphs, the 100% welding efficiency is depicted, i.e., the quotient of the welded specimen strength per the non-welded specimen strength on a % scale. Welding efficiency higher than 100% shows that the weld illustrated increased strength compared to the non-welded specimen (control sample), which is one of the desired responses in welding materials. The graphs presented show the impact of the TS and the welding tool geometry in the process. Welding efficiency higher than 100% was achieved only with the highest TS studied in the work. The specimens welded with the PPD tool had the worst mechanical response in the specific tests. PPA-welded specimens were the second worst, with the TS significantly affecting their strength in this case. Specimens welded through the PPB tool had a superior mechanical response and, from the tensile test graphs, it seems that the TS did not significantly affect their performance, with the samples having a similar response and achieving very close to, or even higher than 100% welding efficiency. The sample welded with the PPC tool with the highest TS of this work achieved the highest strength in the tests, with 120.04% welding efficiency. Overall, the mechanical strength of the welded samples was satisfactory in most cases, and the considerable differences between them prove the need for proper tuning of the welding parameter levels. Throughout the tensile test sequence, in most cases, specimens failed within the seam region, i.e., in Weld Nugget or the Thermomechanically Affected Zone (TMZ). This failure pattern was more or less expected, due to the intrinsic 3DP cavities and the porous structure in this region observed with microscopy and presented and discussed below. Specimens' remaining thickness (RT) at the welding area was

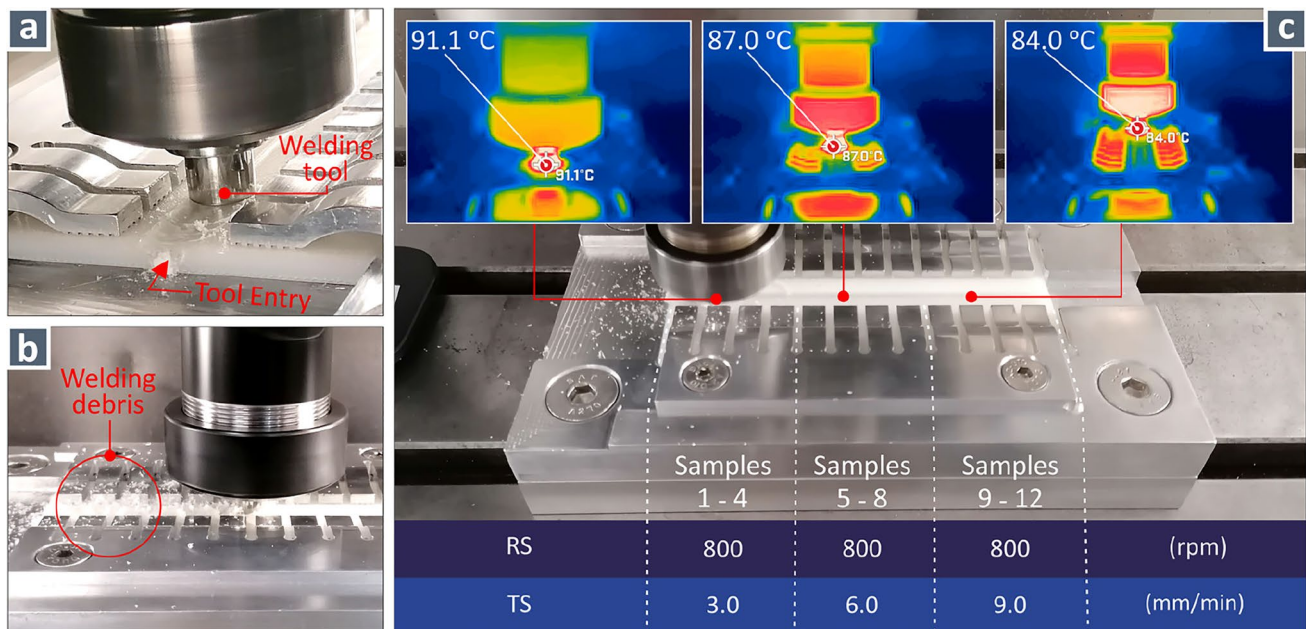


Fig. 3 (a) FSW in the experimental setup of this work, (b) FSW process and the scattering of the surface 3DP texture debris, (c) FSW of the weld specimens with different parameters along the weld seam,

significantly decreased, so despite the satisfactory mechanical strength level, the load-carrying capacity of the specimen was low, owing to the considerable decrease of the cross-section area.

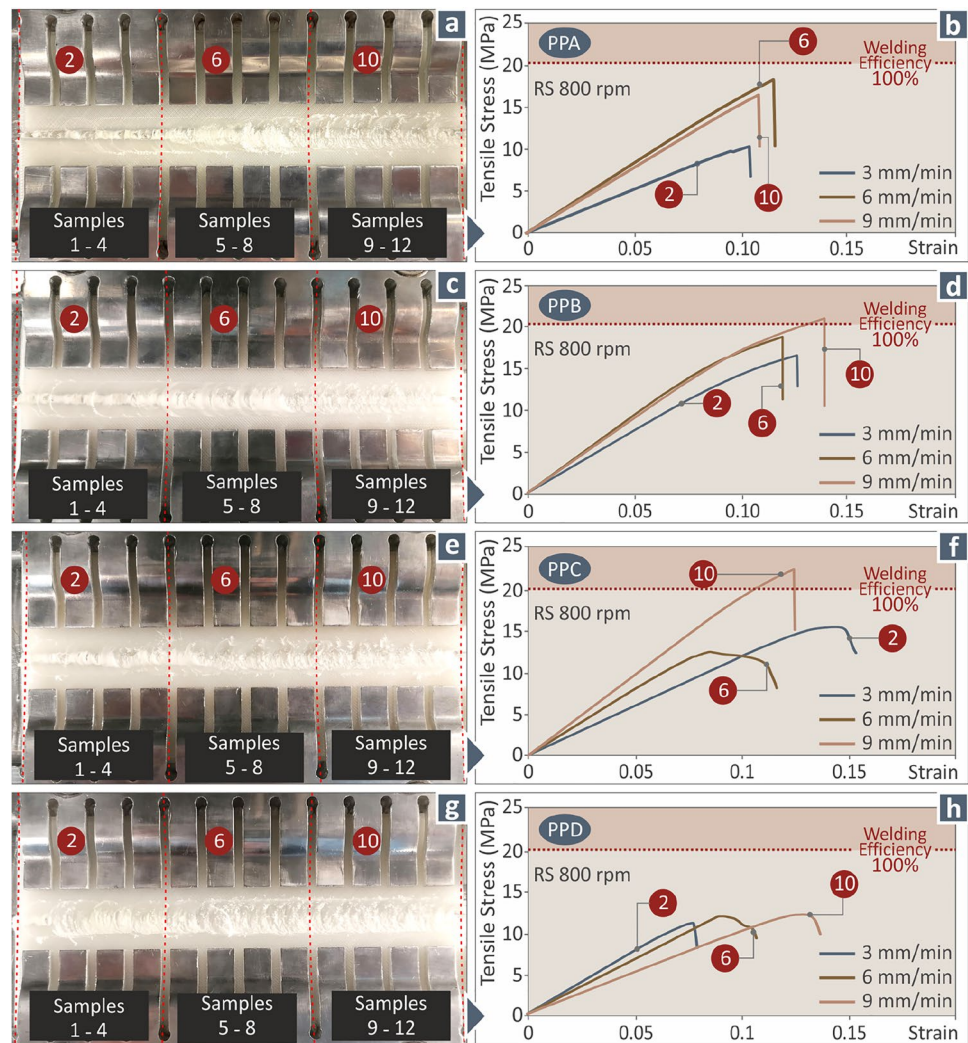
Figure 5 presents stereoscopic and optical microscope images of welded samples (in this case the welding conditions are 600 rpm RS, PPA tool, 9 mm/min TS). Starting from Fig. 5b, the micrograph shows a vertical view, taken from the top of the specimen, which illustrates a joint in its full width. The FSW kinematics is embedded, whereas the contact zone of the shoulder with the two welded specimens is evident. Moreover, Fig. 5a and b illustrate magnifications of the same joint for the advanced side (AS) and retreating side (RTS) respectively. These aspects can offer a first but decisive impression regarding the gradual razing of the 3DP superficial texture, in both the RS and RTS vicinities. Practically, the shoulder edge “cuts” the superficial strands of the workpieces and forms the debris scatter, throughout the course of each FSW experiment (recalling Fig. 3b). Furthermore, a deeper insight into the welding mechanism derives from the micrograph in Fig. 5e. The stereoscopic image is taken vertically to the side (cross-section) surface of the welded samples. The fine-polished surface of the crosscut of the joint visualizes the ensemble of the formed regions (non-welded and welded and unwelded ones), as well as their formation mechanisms. A vitreous nugget zone is formed along the area where the tool pin passes. The formation of the TMZ and the HAZ for both the AS and the RTS is clearly distinguished, owing to the obvious differences

the maximum developed temperature in each case is indicating along with the position it occurred

between them and the appearance of the intrinsic layer-by-layer 3DP structure of the unwelded material. Hereby, the initial internal structure, i.e., built-in polymer strands, makes the welding zones that suffer from FSW thermomechanical stressing plainly visible. The expected decrease of the workpiece thickness within the TMZ, compared to the corresponding one of the original workpieces, is also clearly visible. This phenomenon, which is boosted by the porous structure of the 3D-printed specimens, is a key quality indicator for the FSW joints. The minimum remaining thickness (RT) is along the common edge of the weld samples. More specifically, Fig. 5d presents the porous 3D printing structure in the unwelded part of the sample. The crossing strand formation along with the porosity of the structure is evident. Figure 5f accordingly illustrates the unwelded structure, as well as the formation of the NZ and the TMZ for the RTS of the same joint.

The thorough macro- and micro-inspection of all specimens, in some cases, led to the detection of internal and/or external quality issues and defects, which are usually detectable also in FSW joints of bulk polymeric materials. More specifically, Fig. 6 includes micrographs at joint cross-sections of specimens welded in different welding scenarios and includes at least a defect. In Fig. 6a, cavitations can be observed at the NZ and the TMZ zones, which may be attributed to the trapped air that the laminar 3DP structure of the MEX process intrinsically includes. Nominally, this air is diminished within the welding zone, owing to the thermomechanical conditions occurring there, but in some

Fig. 4 (a) Weld seam (PPA weld tool), (b) stress–strain diagrams for specimens welded at 800 rpm, via the PPA welding tool for all TS levels, (c) weld seam (PPB weld tool), (d) stress–strain diagrams for specimens welded at 800 rpm, through the PPB weld tool for all TS levels, (e) weld seam (PPC weld tool), (f) stress–strain diagrams for specimens welded at 800 rpm, through the PPC weld tool for all TS levels, (g) weld seam (PPD weld tool), (h) stress–strain diagrams for specimens welded at 800 rpm, with the PPD weld tool for all TS levels



cases, air bubbles are further trapped, forming macro- or micro-cavitations within the welding zone. On the other hand, the micrograph of Fig. 6b indicates a considerable non-symmetric surface downside and in addition a visible cavity in the NZ. As mentioned, above, the surface downside is a well-known issue in the FSW of metals and polymers. Especially, in FSW of MEX 3D printed specimens, such behavior is expected to be enhanced, since the material fills the voids and pores of the 3D printing structure, during the welding process. In this case, this downside was formed mainly in the NZ of the RTS and not uniformly in the weld region. In Fig. 6c, surface pits can be observed mainly on the top surface of the sample. The typical FSW regions are also evident in the image. In Fig. 6d, a magnified aspect of the NZ cavitation developed of 6b during the FSW process is inserted. The use of backlight in the specific micrograph enhances the clarity of the cavitation and the 3DP structure with strands.

At this point of morphological inspection and evaluation, it was considered that a deeper perception of the tool pin

geometry effect on the joints' formation would be supportive. From this perspective, stereoscopic and optical micrographs in Fig. 7 describe the findings for samples joined together by keeping the FSW parameters intact (in this case 600 rpm, 9 mm/min), for each of the four different welding tools. Differences can be observed in the formation of the FSW zones among the different samples. In the PPA tool (Fig. 7a), the nugget is almost cylindrical and extends to all the sample's thickness. In the PPB tool (Fig. 7b), the NZ does not have a cylindrical shape, still again it extends to the bottom of the sample. In the samples welded with the threaded tools, the nugget does not extend to the bottom of the samples as well. In the PPC tool (Fig. 7c), it has a rather cylindrical shape, which widens as it reaches the top surface of the sample, while in the PPD tool (Fig. 7d), it has a frustum shape, also widening at the top of the sample. The TMZs also differ in their width and thickness from the top of the samples. The TMZ on the sample welded with the PPA tool (Fig. 7a) is the thickest among the samples (depth from the top surface of the sample). It abruptly narrows and

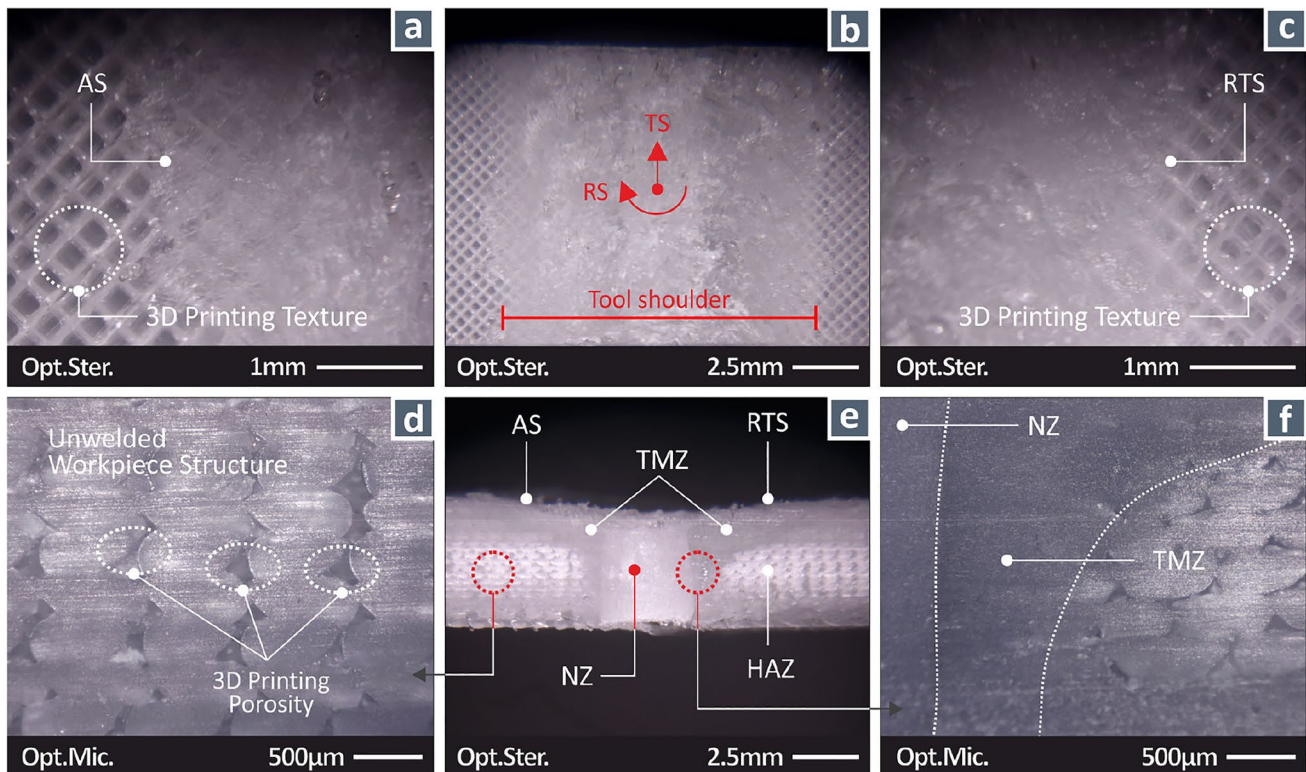


Fig. 5 Specimen welded with 600 rpm, PPA tool, 9 mm/min TS, Top view: (a) Left side of the TMZ 2.5× stereoscopic image (advanced side), (b) weld nugget, 0.8× stereoscopic image, (c) right side of the TMZ, 2.5× stereoscopic image (retreating side), (d) side surface non-

welded area, optical microscope 5.0× (e) welding zone, 0.8× stereoscopic image, (f) specimen welded with 600 rpm, PPB tool, 9 mm/min TS, optical microscope 5.0×, the side surface of the TMZ, the characteristic zones (NZ and TMZ) are outlined in the figure

becomes the narrowest among the samples at about 30% of the sample's thickness from the top. The TMZ on the left and the right of the NZ have differences in their shape. In the PPB tool (Fig. 7b) the TMZ has a rather uniform thickness and similar shape on both sides of the NZ. A similar shape in the TMZ is observed on the sample welded with the PPD tool (Fig. 7d). The most asymmetrical shape is observed in the TMZ of the sample welded with the PPC tool (Fig. 7c). Regarding the samples' top surface downside (which is common in FSW in the samples), this is more intense in the samples welded with the threaded tools (PPC and PPD), with the highest lowering of the surface observed in the sample welded with the PPC tool. The optical microscope images (Fig. 7b, e, h, k) present the TMZ and the transitional region to the 3D printed, not-welded, structure. In these images, again the NZ and the TMZ are clearly observed and outlined in the samples. The 3D printing strands can be observed outside the FSW region, along with the expected porosity of the 3D printing structure. The differences in the shape and the size of the NZs and the TMZs between the samples welded by the different tools are again obvious. Figure 7c, f, i, and l present micrographs taken from the top of the samples, after the completion of the tensile tests, to evaluate their

failure mode. In these images, it is shown that the samples in all cases failed in the TMZ or were close to it. There are significant differences in the failure of the samples, with samples welded with the PPA and the PPB tools exhibiting a brittle failure, while samples welded with the PPC and the PPD tools exhibiting a more ductile failure, with deformation shown in the material and rough surfaces produced in the fracture region. Again, the NZ and the TMZ can be observed. In these regions, the 3D printing strands were unified during the FSW process. Overall, it can be observed, that the samples welded with tools without threads fail in a more brittle way, while samples welded with threaded tools exhibit a more ductile failure. This manner was also confirmed in the SEM images taken in the work.

Figure 8 shows Scanning Electron Microscopy (SEM) images from the top of the samples, welded by the four different tools of the study, at the TMZ. All images were taken on the advancing side of the sample. The strand trajectories outside the HAZ are visible in all cases. The TMZ and the overall morphology in the weld regions significantly differ between the samples, welded with the different weld tools. More specifically, the sample welded with the PPA tool (Fig. 8a) exhibits a smoother upper

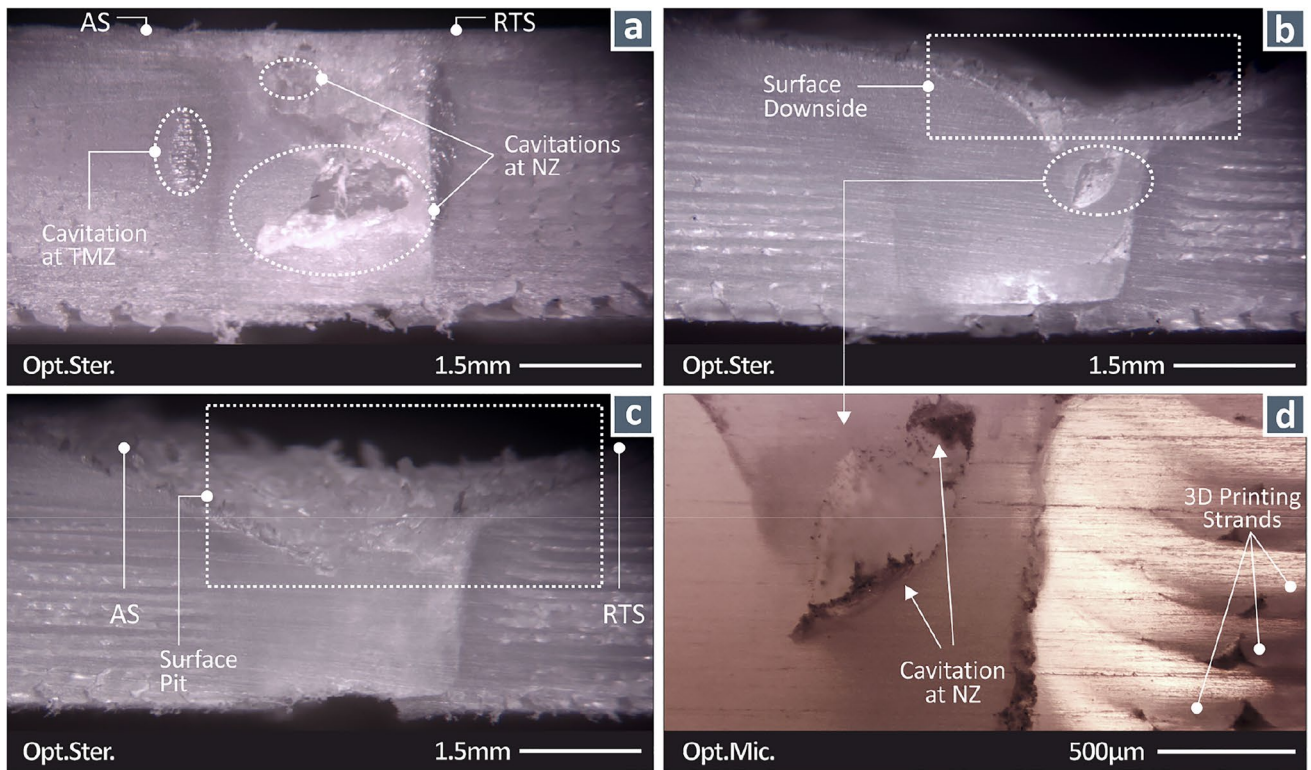


Fig. 6 Side surface of the weld region: (a) PPA, 600 rpm, 6 mm/min, stereoscopic image 1.5 \times , (b) PPC, 600 rpm, 6 mm/min, stereoscopic image 1.5 \times , (c) PPA, 800 rpm, 9 mm/min, stereoscopic image 1.5 \times , (d) PPA, 600 rpm, 6 mm/min, microscope image 5.0 \times

surface. The rougher and more asymmetrical upper surface is observed in the sample welded with the PPB tool (Fig. 8b). In the samples welded with the PPC (Fig. 8c) and the PPD (Fig. 8d) tool, the upper surface of the weld region shows a rather similar morphology, with the PPD sample presenting a rougher surface. Welding debris is also visible in the images. A thickness dropping can also be observed on the side of the samples.

The fractured surface of samples welded with the four different tools of the study is further presented in Fig. 9. These images verify the fracture mechanism initially identified in Fig. 7 microscopy images. Samples welded with the PPA (Fig. 9a) and the PPB tool (Fig. 9b) show a more brittle behavior in the fracture area, with minimum deformation of the material. Samples welded with the PPC (Fig. 9c) and the PPD tool (Fig. 9d) show a more ductile behavior (deformation of the material is decreased in the fracture area), with visible deformation in the fracture area.

As mentioned above, throughout the FSW process, the temperature was monitored, to evaluate the state of the material. In all cases, it was confirmed that the solid state of the material was maintained. To document the thermal properties of the material, TGA and DSC analyses were performed. The produced diagrams are shown in Fig. 10a and b respectively. In the TGA, it was found that the material

starts to degrade at 250 °C. In the DSC analysis, the melting temperature of the material was determined to be 225 °C. The maximum recorded temperatures in all the conducted experiments are shown in Fig. 10b. The TGA graph shows that the 3D printing temperature used to build the specimens did not cause any degradation in the material. At the same time, the correlation between the TGA and DSC graphs with the maximum temperatures recorded in the study indicates the maximum temperature in all the FSW experiments (~150 °C). Such temperature levels are much lower than the temperature the material starts to degrade and much lower than its melting point as well. This verifies that the polymer during the FSW experiments was in a solid state.

3.2 Aggregated response results and parameters analysis

Table 2 lists average values along with their deviation, for each experimental run, i.e., Residual Thickness (mm), Welding Temperature (°C), sB (Mpa), welding efficiency (sB/sB Ref. %), E (Mpa), and Tensile Toughness (MJ/m³). The analytical results of the experiment are presented in the supplementary data for this work in Appendix Table 1.

In the main effect plots (see Fig. 11), the PPC exhibits the best performance regarding the tensile strength and

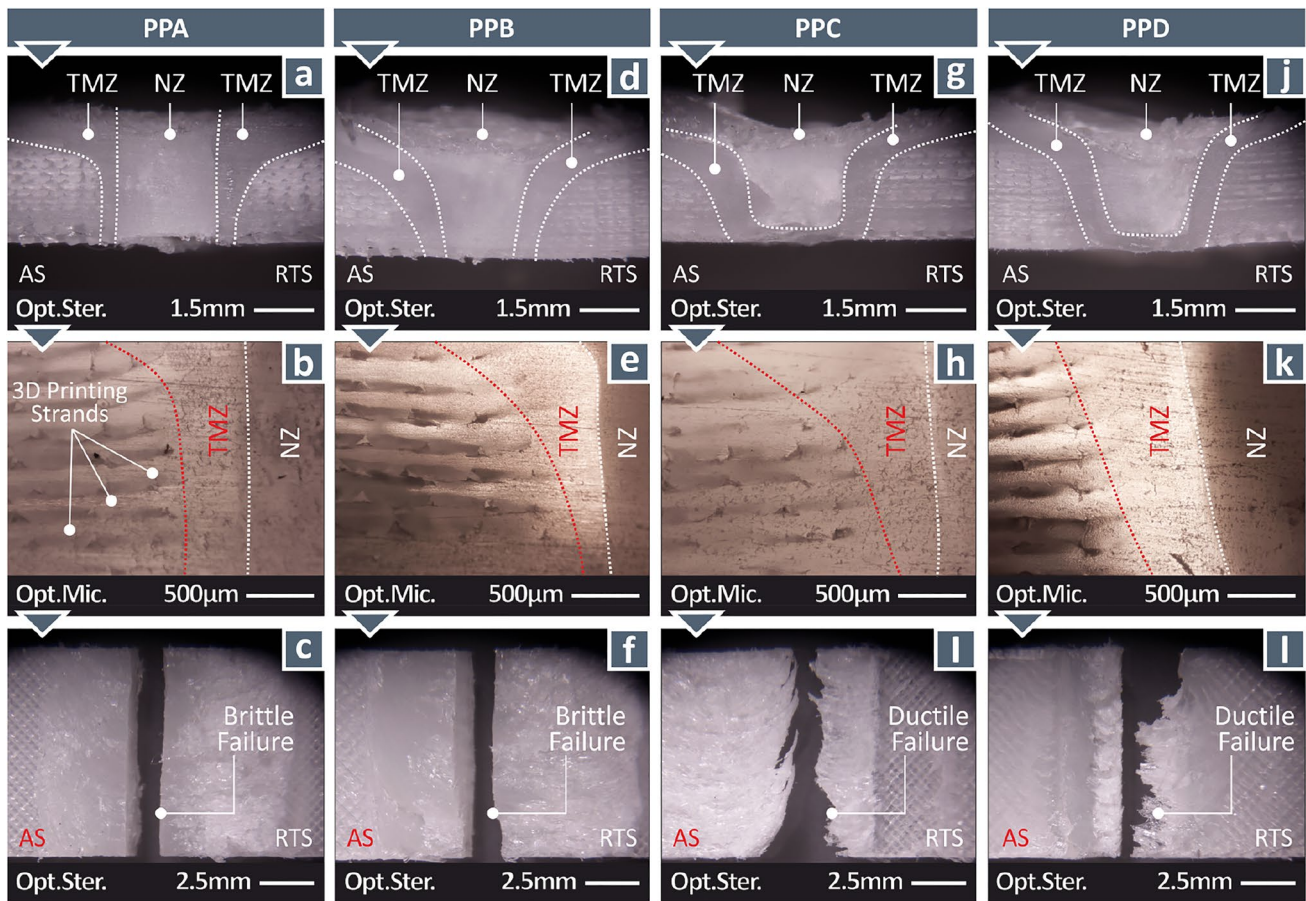


Fig. 7 Stereoscopic and optical microscope images of samples welded with the four tools of this work at 600 rpm and 9 mm/min: (a)–(c) PPA, (d)–(f) PPB, (g)–(i) PPC, (j)–(l) PPD. (a), (d), (g), (j) are 1.5× stereoscopic images of the side surface of samples, (b), (e),

(h), and (k) are 5.0× optical microscope images of the side surface of a sample, (c), (f), (i), (l) are 0.8× stereoscopic image captured from the side of the fracture samples

elasticity modulus. At the same time, the 1000 rpm gives the highest sB and lowest temperatures with moderate E, while 9 mm/min travel speed, optimizing the sB and E and minimizing the temperatures. Overall, RS seems to be the most dominant control parameter of the process, while the tool geometry and the TS do not significantly affect the process. The following were observed on the MEPs:

- Residual thickness is not significantly affected by the weld tool or the TS. Higher residual thickness values are achieved with low RS (highest value at 600 rpm), which is ranked as the 1 parameter affecting the Residual Thickness.
- WT has higher values with the PPB tool and the lowest values with the PPD tool, with the weld tool being the no 1 parameter in the rank in this case. TS is ranked no 2 and RS no 3, with both parameters not significantly affecting

the WT. Higher values are observed at lower RS and TS and lower values at higher RS and TS.

- TS is ranked as the no 1 parameter for the sB, with the highest values achieved at high TS values, which is the desired outcome. Medium RS achieved the highest sB values. The lowest sB values are reported for 600 rpm, the lowest RS studied, while high RS also resulted in decreased sB values. Regarding the welding tool, PPC achieved the highest sB, then PPB, and PPA. The lowest response is reported with the PPD tool. Still, the weld tool was ranked as the no 3 parameter.
- Regarding the modulus of elasticity, TS is not a significant parameter. Same with the sB, PPC achieved the highest sB, then PPB, with the remaining tools following in this classification. The RS was the significant parameter regarding the E, with high RS (1200 rpm) achieving the highest response, and the lowest response was reported in the lowest RS studied (600 rpm).

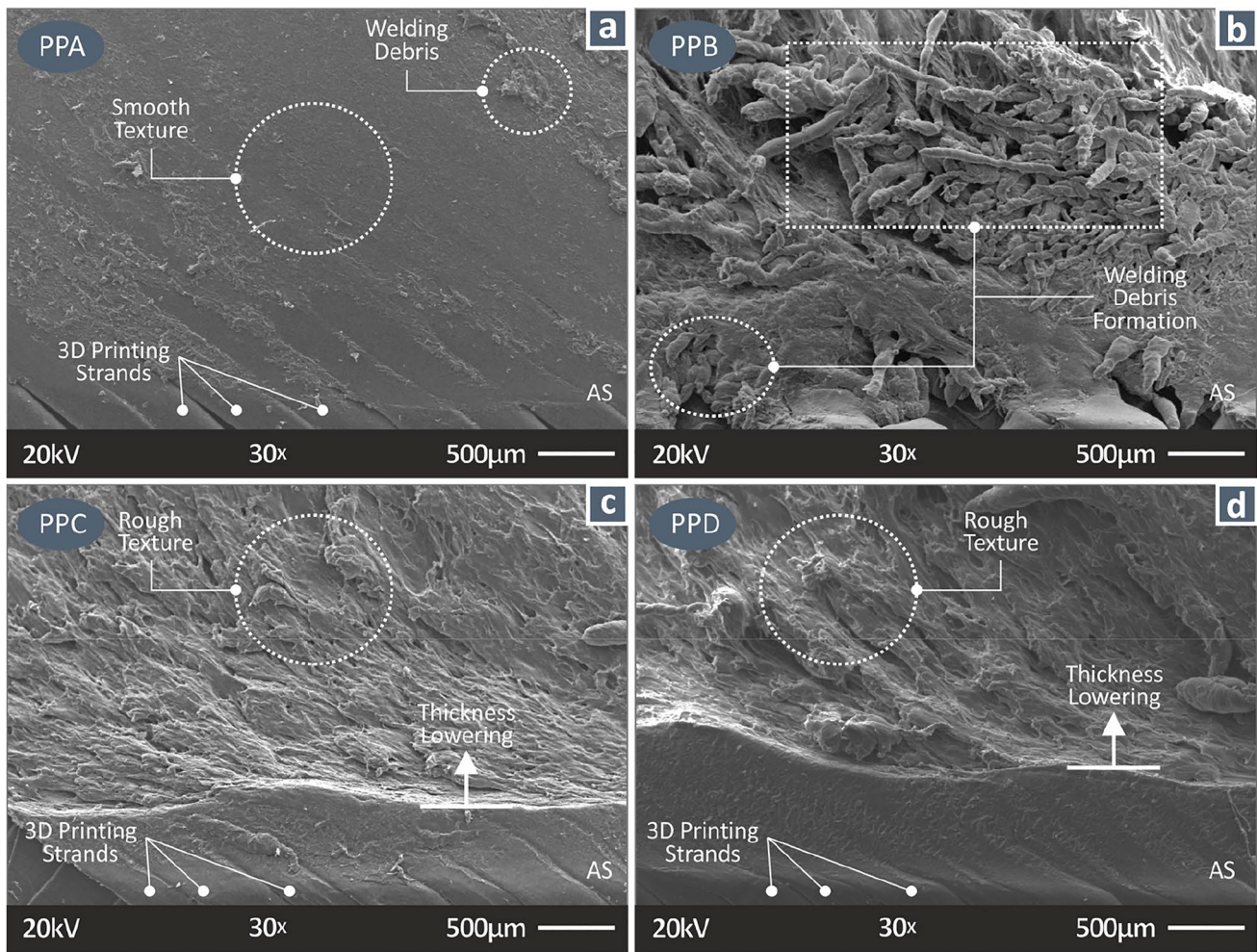


Fig. 8 30×SEM images from the top of the samples in the TMZ: (a) PPA tool, 600 rpm, 6 mm/min, (b) PPB tool, 600 rpm, 9 mm/min, (c) PPC tool, 600 rpm, 9 mm/min, (d) PPD tool, 600 rpm, 9 mm/min

It should be mentioned that no control parameters combination optimizes all the response parameters. It depends on the desired outcome to select the proper set of parameters in each case. Also, these observations are for the specific control parameters range in their values.

MEP diagrams offer no insight into the relationships between the control parameters, (synergistic or antagonistic relations). Therefore, to evaluate such mechanisms, the interaction plots were formed, to show the complex interaction between all process parameters for E, sB, and WT (see Fig. 12).

- All control parameters interact synergistically for the Residual Thickness response parameter.
- Rotational speed and travel speed interact synergistically according to the E and are antagonistic for the sB and WT.
- Tool interacts antagonistically with rotational and travel speeds for all the outputs (E, sB, and WT).

Modulus of elasticity E:

- Fig. 12 shows that the 800 and 1000 rpm of the RS give the same modulus of elasticity for all weld tools, while 1200 rpm is better for the PPC tool.
- 6 and 9 mm/s travel speed gives better E for all weld tools except the PPD where 3 mm/s gives better E.
- Higher rotational speeds give a better modulus of elasticity for all travel speeds.

Ultimate tensile strength:

- The higher sB is presented at 1000 rpm for the PPC tool, while at 1200 rpm, the PPC tool gives the best sB.
- PPB tool gives the best sB values for 9 mm/s, while 9 mm/s optimizes all tools' sB performance.
- 9 mm/s travel speed optimizes all rotational speeds, 1000 rpm and 9 mm/s give the higher sB.

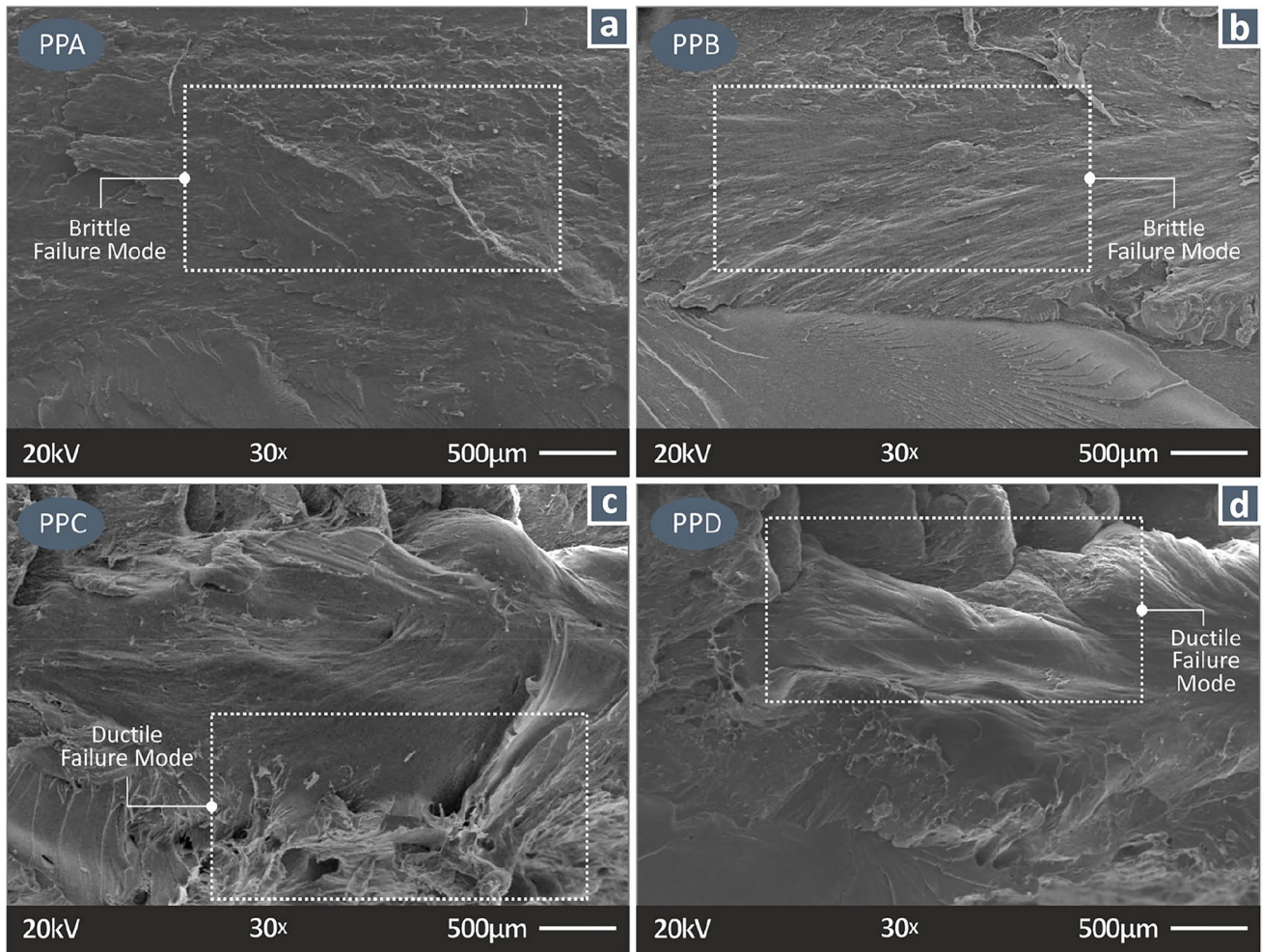


Fig. 9 30×SEM images from the fracture surface of the samples welded with the four different tools of the study: (a) PPA tool, 600 rpm, 6 mm/min, (b) PPB tool, 600 rpm, 9 mm/min, (c) PPC tool, 600 rpm, 9 mm/min, (d) PPD tool, 600 rpm, 9 mm/min

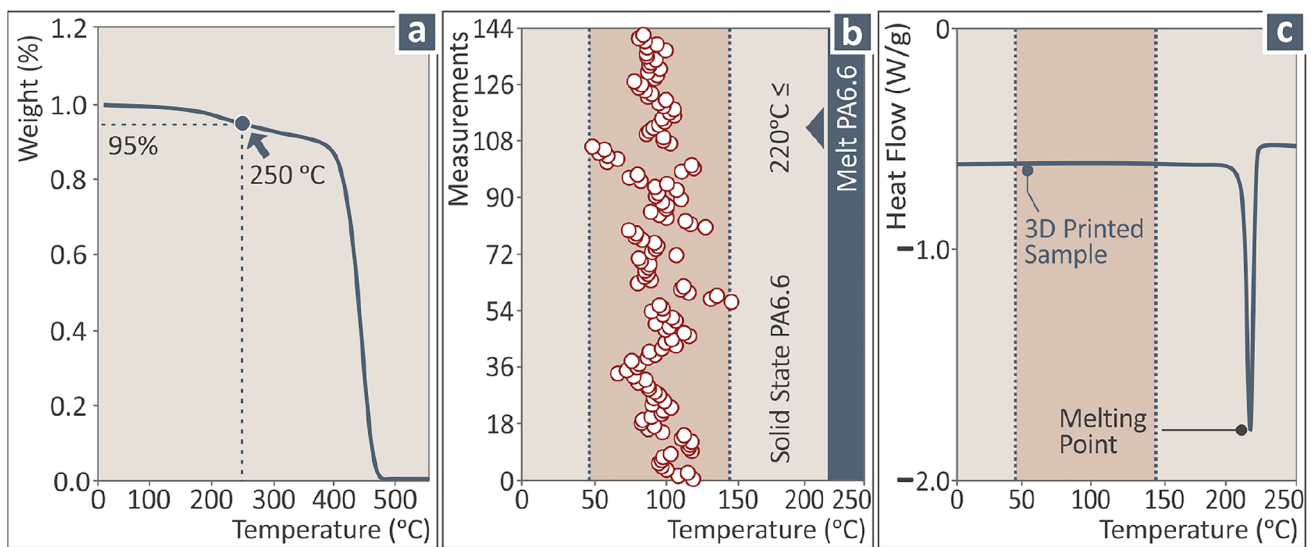
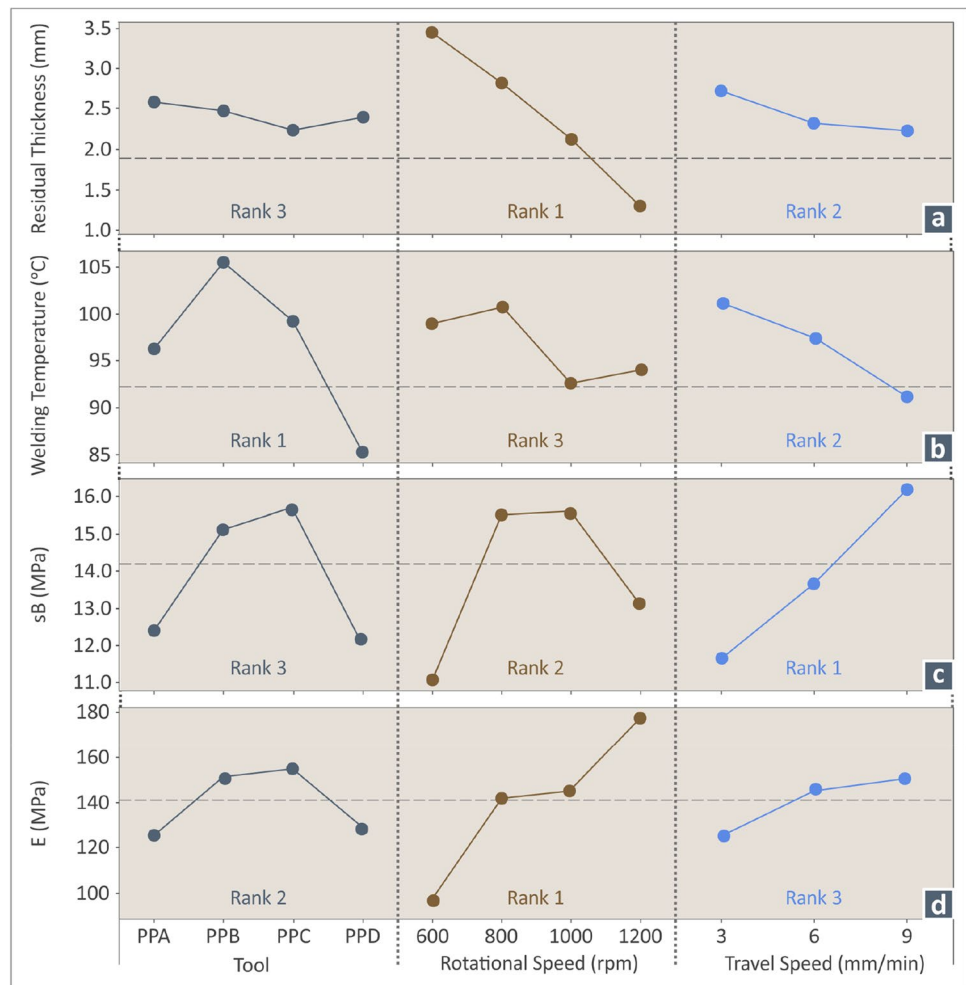


Fig. 10 (a) TGA graph, (b) recorded maximum temperature values during the FSW process, (c) DSC graph

Table 2 Mean values and standard deviation of measured responses for each experimental run

Run	Residual thickness (mm)	Welding temperature (°C)	sB (Mpa)	sB/sB Ref. (%)	E (Mpa)	Toughness (MJ/m ³)
1	3.90±0.01	116.13±5.22	6.01±0.55	29.53±2.71	80.46±3.19	0.24±0.13
2	3.85±0.03	99.10±2.72	14.66±1.04	72.11±5.09	94.16±5.70	1.29±0.11
3	3.12±0.07	101.07±3.44	17.46±0.90	85.88±4.43	125.43±3.92	1.26±0.67
4	3.73±0.16	80.50±2.69	9.90±1.12	48.71±5.50	101.96±4.67	0.42±0.21
5	3.11±0.50	90.90±2.76	18.20±1.15	89.50±5.68	164.34±4.23	0.87±0.34
6	2.84±0.14	102.87±5.13	15.98±1.16	78.59±5.70	154.44±1.73	0.68±0.29
7	2.50±0.10	98.40±9.29	3.81±0.30	18.74±1.45	58.34±6.70	0.92±0.70
8	1.99±0.13	91.40±5.75	15.21±1.53	74.81±7.54	157.19±7.71	2.36±0.65
9	1.96±0.33	78.60±2.88	20.15±1.53	99.07±7.52	189.72±11.50	3.96±0.83
10	1.46±0.67	101.50±2.77	11.78±1.37	57.95±6.74	89.69±1.55	0.93±0.89
11	0.88±0.69	90.17±2.47	4.59±0.57	22.57±2.79	123.87±5.54	0.38±0.20
12	1.63±0.09	98.70±2.05	11.09±1.90	54.51±9.34	167.09±19.22	3.75±4.06
13	3.86±0.07	118.83±1.05	3.65±0.24	17.94±1.20	60.44±3.47	0.12±0.08
14	3.64±0.14	115.60±3.75	12.62±0.99	62.06±4.87	115.12±5.67	1.32±0.66
15	3.20±0.08	93.97±4.97	14.94±0.25	73.47±1.25	116.34±1.82	1.23±0.48
16	3.64±0.13	112.83±6.27	16.63±0.75	81.75±3.67	124.99±15.48	1.26±0.71
17	2.88±0.03	99.93±5.09	19.08±0.94	93.80±4.64	149.97±5.63	2.34±1.58
18	2.79±0.05	104.67±4.74	20.81±1.25	102.33±6.16	142.20±5.79	3.88±1.46
19	2.13±0.03	121.33±7.38	16.06±0.95	78.98±4.68	157.81±8.90	2.55±0.76
20	2.04±0.17	96.57±5.55	20.45±1.04	100.54±5.11	168.05±8.36	2.63±0.60
21	2.09±0.05	101.13±1.87	21.02±1.29	103.35±6.36	163.11±7.24	2.12±0.27
22	1.14±0.25	106.33±1.77	10.55±1.22	51.87±6.01	192.00±18.36	0.50±0.14
23	1.05±0.11	99.40±2.49	12.15±0.42	59.75±2.04	213.92±9.49	0.58±0.10
24	1.27±0.12	89.10±2.41	13.42±0.82	65.97±4.05	214.85±3.66	0.78±0.51
25	3.81±0.03	87.03±3.81	15.77±1.51	77.52±7.42	76.52±5.96	0.56±0.35
26	3.29±0.33	101.27±3.57	10.94±1.54	53.79±7.55	89.50±4.56	0.80±0.55
27	2.45±0.07	95.23±4.68	9.96±1.20	48.99±5.90	99.86±2.66	1.10±0.35
28	3.51±0.29	95.97±4.02	15.34±1.04	75.43±5.11	120.53±6.28	0.92±0.32
29	2.25±0.08	139.67±7.45	12.57±0.74	61.80±3.66	160.93±3.43	0.95±0.18
30	2.05±0.09	114.67±2.73	22.35±1.02	109.92±5.00	195.22±16.68	3.81±1.63
31	2.20±0.28	101.03±9.80	11.17±1.45	54.91±7.13	135.61±6.48	1.15±0.66
32	1.81±0.15	101.87±7.71	15.59±1.16	76.67±5.69	150.92±6.24	2.43±0.13
33	1.92±0.06	80.43±4.17	20.28±0.48	99.75±2.38	169.94±7.01	4.05±0.15
34	1.28±0.04	82.07±2.62	23.04±1.26	113.31±6.18	243.14±10.98	4.11±1.02
35	0.83±0.45	92.67±3.40	14.97±0.66	73.63±3.27	238.96±16.29	2.22±1.82
36	1.44±0.07	92.70±4.03	16.52±1.31	81.23±6.43	181.54±5.50	3.69±0.84
37	3.47±0.51	93.37±3.67	9.26±1.06	45.51±5.21	120.45±3.30	0.37±0.24
38	3.82±0.02	86.03±3.59	9.08±1.04	44.67±5.10	93.07±4.45	0.77±0.28
39	2.82±0.12	73.47±5.56	8.81±0.47	43.34±2.33	92.14±3.70	0.92±0.46
40	2.33±0.12	86.50±4.65	10.97±0.65	53.93±3.21	155.11±7.12	0.71±0.11
41	2.36±0.08	88.43±1.25	12.38±1.60	60.88±7.88	133.08±4.84	0.83±0.10
42	2.37±0.17	85.47±4.10	11.78±0.77	57.91±3.80	102.71±6.41	0.88±0.15
43	2.64±0.49	117.97±4.63	10.52±1.45	51.75±7.14	133.98±5.56	2.24±0.89
44	2.05±0.09	62.57±4.10	15.82±0.99	77.77±4.88	133.86±5.75	3.54±0.13
45	2.15±0.10	54.00±4.30	17.17±0.61	84.44±2.98	123.72±5.91	4.96±0.43
46	1.80±0.16	90.13±3.70	12.24±1.07	60.18±5.27	154.71±6.79	2.30±0.31
47	1.29±0.31	95.00±6.60	10.18±0.68	50.05±3.35	138.63±9.81	0.70±0.39
48	1.55±0.04	84.97±2.22	17.07±0.94	83.92±4.64	172.44±10.39	2.79±0.87

Fig. 11 Main effect plots for (a) E, (b) sB, and (c) WT



Welding temperature:

- Lower WT presented at 1000 rpm for tool PPD, while 800 rpm for tool PPC gave higher temperatures. Here it seems that the higher temperatures resulted in better tensile strength.
- 9 mm/s TS gives a lower WT for all tools while 3 mm/min gives a higher WT for the PPB tool and 9 mm/s is the lowest for the PPD tool.
- 3 mm/s and 1000 rpm give the higher WT, while 9 mm/s and 1000 rpm provide the lowest. 1000 rpm shows a higher variability according to the WT.

The interaction plots verified the complexity of the relationships between the three control parameters with respect to the response parameters studied. Deterministic mathematical models are insufficient to describe them or, predict their effect on the response parameters.

3.3 ANOVA analysis and modeling

The Separated Cubic Regression Model (SCRM) for each response is calculated by the following sets of four equations (one per categorical predictor, e.g., for welding tools PPA, PPB, PPC, and PPD in question, herein):

$$Y_{A,k} = b_{A,k} + \sum_{i=1}^n b_{A,i,k}x_i + \sum_{i=1}^n c_{A,i,k}x_i^2 + \sum_{i=1}^n d_{A,i,k}x_i^3 + \sum_i \sum_j e_{A,i,j,k}x_i^m x_j^n + f_{A,k} \quad (1)$$

$$Y_{B,k} = b_{B,k} + \sum_{i=1}^n b_{B,i,k}x_i + \sum_{i=1}^n c_{B,i,k}x_i^2 + \sum_{i=1}^n d_{B,i,k}x_i^3 + \sum_i \sum_j e_{B,i,j,k}x_i^m x_j^n + f_{B,k} \quad (2)$$

$$Y_{C,k} = b_{C,k} + \sum_{i=1}^n b_{C,i,k}x_i + \sum_{i=1}^n c_{C,i,k}x_i^2 + \sum_{i=1}^n d_{C,i,k}x_i^3 + \sum_i \sum_j e_{C,i,j,k}x_i^m x_j^n + f_{C,k} \quad (3)$$

$$Y_{D,k} = b_{D,k} + \sum_{i=1}^n b_{D,i,k}x_i + \sum_{i=1}^n c_{D,i,k}x_i^2 + \sum_{i=1}^n d_{D,i,k}x_i^3 + \sum_i \sum_j e_{D,i,j,k}x_i^m x_j^n + f_{D,k} \quad (4)$$

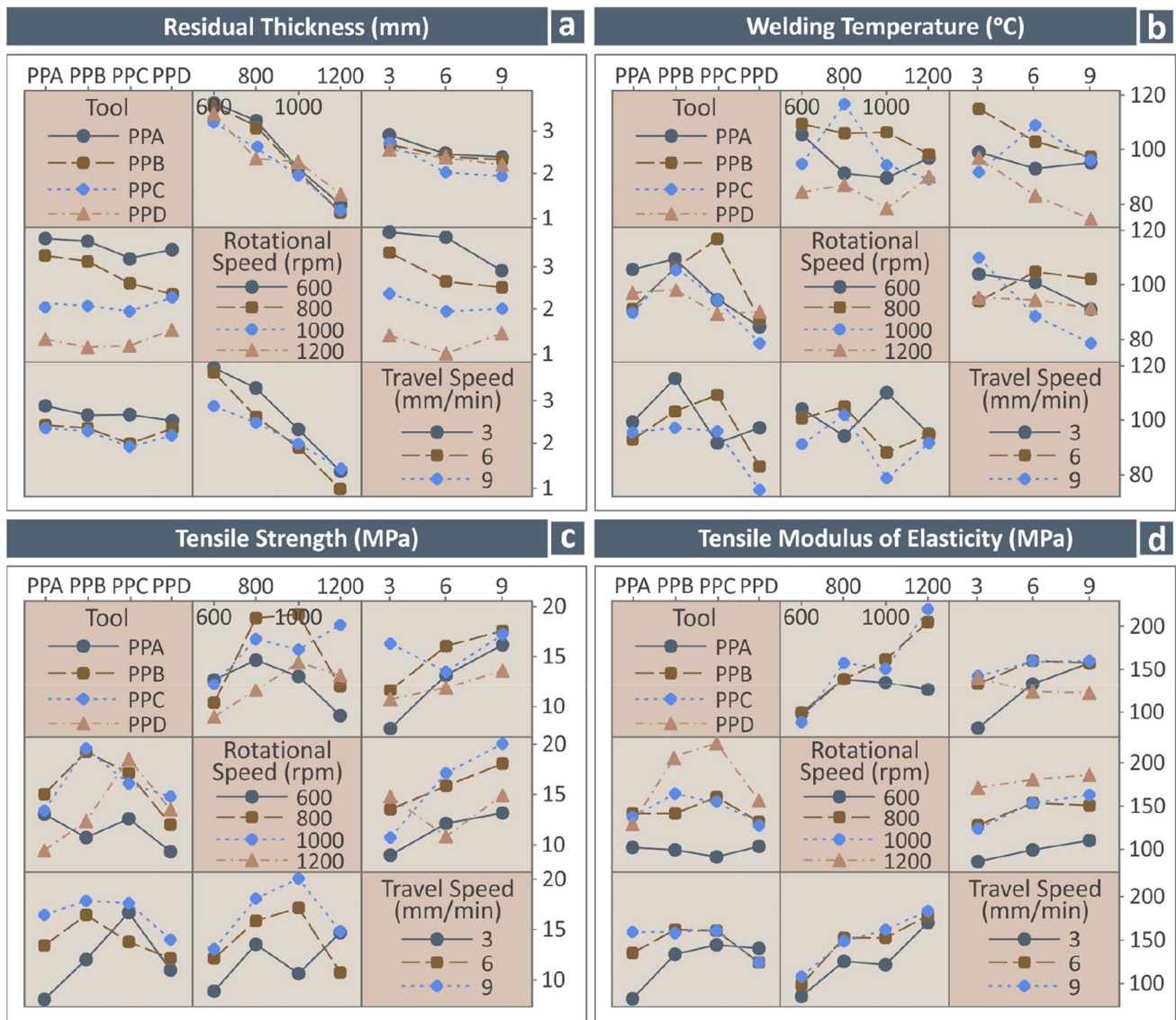


Fig. 12 Interaction plot charts

Were, k represents the response output (e.g., Residual Thickness, Welding Temperature, Tensile Strength, Elasticity Modulus, and Tensile Toughness), a is the constant value, b the coefficients of the linear terms, c the coefficients of the quadratic terms, d the coefficients of the cubic terms, e the coefficients of the cross-product terms (exponents n and m take integer values from 0 up to 3), f the error and ξ_i the two ($n = 2$) continuous control parameters, i.e., Travel Speed and Rotational Speed.

Table 3 presents the ANOVA for the Residual Thickness vs. the control parameters RS, TS, and Tool. The regression F-value is 45.34 (> 4) and the P -value is almost zero. R values are higher than 89.87%. These results indicate that the model is more than sufficient for the prediction of Residual Thickness. For each welding tool, an equation was

compiled for the prediction of the Residual Thickness, as a function of the control parameters RS and TS (Eqs. (5)–(8) respectively). These equations were formed by analyzing the determined results and by following the corresponding literature on the operating mechanisms of these models [73].

Table 4 presents the corresponding ANOVA for the tensile strength vs the control parameters RS, TS, and Tool. The regression F-value is 54.73 (> 4) and the P -value is almost zero. R values are higher than 91.75%. These results indicate that the model is more than adequate for the prediction of the tensile strength, which is overall the most critical among the responses considered in the work. For each welding tool, an equation was compiled for the prediction of the tensile strength, as a function of the control parameters RS and TS (Eqs. (9)–(12) respectively).

Table 3 Polynomial ANOVA, residual thickness vs. RS, TS, tool

Source	DF	Adj SS	Adj MS	F-value	P-value
Regression	44	114.058	2.59222	45.34	0.000
RS	1	0.387	0.38696	6.77	0.011
TS	1	0.330	0.32977	5.77	0.018
Tool	3	1.060	0.35347	6.18	0.001
RS ²	1	0.364	0.36426	6.37	0.013
TS ²	1	0.336	0.33628	5.88	0.017
RS•TS	1	0.304	0.30370	5.31	0.023
RS×Tool	3	1.301	0.43382	7.59	0.000
TS×Tool	3	0.183	0.06102	1.07	0.367
RS ² ×RS	1	0.336	0.33640	5.88	0.017
RS ² ×TS	1	0.281	0.28053	4.91	0.029
RS×TS ²	1	0.308	0.30812	5.39	0.022
RS ² ×Tool	3	1.414	0.47120	8.24	0.000
RS×TS×Tool	3	0.405	0.13497	2.36	0.076
TS ² ×Tool	3	0.115	0.03844	0.67	0.571
RS ³ ×TS	1	0.270	0.26992	4.72	0.032
RS ² •TS ²	1	0.289	0.28946	5.06	0.027
RS ² ×Tool	3	1.405	0.46846	8.19	0.000
RS ² ×TS×Tool	3	0.639	0.21305	3.73	0.014
RS×TS ² ×Tool	3	0.084	0.02785	0.49	0.692
RS ³ ×TS ²	1	0.286	0.28589	5.00	0.028
RS ² ×TS×Tool	3	0.739	0.24621	4.31	0.007
RS ² ×TS ² ×Tool	3	0.074	0.02473	0.43	0.730
Lack-of-Fit	3	0.124	0.04149	0.72	0.543
Pure Error	96	5.536	0.05767		
Total	143	16.57			
R ²		95.27%			
R ² (adj)		93.17%			
R ² (pred)		89.87%			

Table 4 Polynomial ANOVA, tensile strength vs. RS, TS, tool

Source	DF	Adj SS	Adj MS	F-value	P-value
Regression	44	3109.62	70.673	54.73	0.000
RS	1	104.06	104.060	80.58	0.000
TS	1	47.74	47.736	36.97	0.000
Tool	3	33.73	11.244	8.71	0.000
RS ²	1	120.70	120.703	93.47	0.000
TS ²	1	17.08	17.080	13.23	0.000
RS•TS	1	56.26	56.264	43.57	0.000
RS×Tool	3	32.95	10.984	8.51	0.000
TS×Tool	3	18.68	6.227	4.82	0.004
RS ² ×RS	1	139.75	139.746	108.22	0.000
RS ² ×TS	1	70.52	70.523	54.61	0.000
RS×TS ²	1	21.72	21.724	16.82	0.000
RS ² ×Tool	3	40.48	13.495	10.45	0.000
RS×TS×Tool	3	17.09	5.696	4.41	0.006
TS ² ×Tool	3	38.68	12.893	9.98	0.000
RS ³ ×TS	1	87.85	87.849	68.03	0.000
RS ² •TS ²	1	29.84	29.841	23.11	0.000
RS ² ×Tool	3	52.95	17.651	13.67	0.000
RS ² ×TS×Tool	3	30.64	10.213	7.91	0.000
RS×TS ² ×Tool	3	50.85	16.951	13.13	0.000
RS ³ ×TS ²	1	40.47	40.469	31.34	0.000
RS ² ×TS×Tool	3	62.06	20.685	16.02	0.000
RS ² ×TS ² ×Tool	3	60.51	20.168	15.62	0.000
Lack-of-Fit	3	17.94	5.979	5.22	0.002
Pure Error	96	109.90	1.145		
Total	143				
R ²		96.05%			
R ² (adj)		94.30%			
R ² (pred)		91.75%			

$$\begin{aligned}
 \text{PPA Thicknes} = & -5.520 \cdot 10^2 + 2.034 \cdot 10^{-1}RS + 1.800 \cdot 10^1TS - 2.243 \cdot 10^4RS^2 \\
 & - 1.467TS^2 - 6.033 \cdot 10^{-2}RS \cdot TS + 7.954 \cdot 10^{-8}RS^3 + 6.568 \cdot 10^{-5}RS^2 \cdot TS \\
 & + 4.871 \cdot 10^{-3}RS \cdot TS^2 - 2.375 \cdot 10^{-8}RS^3 \cdot TS - 5.343 \cdot 10^{-6}RS^2 \cdot TS^2 \\
 & + 1.957 \cdot 10^{-9}RS^3 \cdot TS^2
 \end{aligned} \tag{5}$$

$$\begin{aligned}
 \text{PPB Thicknes} = & -7.110 \cdot 10^2 + 2.655 \cdot 10^{-1}RS \\
 & + 2.147 \cdot 10^1TS - 2.973 \cdot 10^{-4}RS^2 \\
 & - 1.485TS^2 - 7.437 \cdot 10^{-2}RS \cdot TS + 1.054 \cdot 10^{-7}RS^3 \\
 & + 8.184 \cdot 10^{-3}RS^2 \cdot TS + 5.069 \cdot 10^{-3}RS \cdot TS^2 \\
 & - 2.907 \cdot 10^{-8}RS^3 \cdot TS - 5.530 \cdot 10^{-6}RS^2 \cdot TS^2 \\
 & + 1.957 \cdot 10^{-9}RS^3 \cdot TS^2
 \end{aligned} \tag{6}$$

$$\begin{aligned}
 \text{PPC Thicknes} = & -6.780 \cdot 10^2 + 2.519 \cdot 10^{-1}RS \\
 & + 2.317 \cdot 10^1TS - 2.790 \cdot 10^4RS^2 \\
 & - 1.559TS^2 - 7.951 \cdot 10^{-2}RS \cdot TS \\
 & + 9.839 \cdot 10^{-8}RS^3
 \end{aligned} \tag{7}$$

$$\begin{aligned}
 & + 8.630 \cdot 10^{-5}RS^2 \cdot TS + 5.212 \cdot 10^{-3}RS \cdot TS^2 \\
 & - 3.047 \cdot 10^{-8}RS^3 \cdot TS - 5.571 \cdot 10^{-6}RS^2 \cdot TS^2 \\
 & + 1.957 \cdot 10^{-9}RS^3 \cdot TS^2 \\
 \text{PPD Thicknes} = & + 4.200 \cdot 10^1 - 1.930 \cdot 10^{-2}RS + 1.649 \cdot 10^1TS \\
 & + 3.442 \cdot 10^{-5}RS^2 - 1.789TS^2 \\
 & - 4.982 \cdot 10^{-2}RS \cdot TS - 1.587 \cdot 10^{-8}RS^3 \\
 & + 4.955 \cdot 10^{-5}RS^2 \cdot TS + 5.574 \cdot 10^{-3}RS \cdot TS^2 \\
 & - 1.660 \cdot 10^{-8}RS^3 \cdot TS - 5.718 \cdot 10^{-6}RS^2 \cdot TS^2 \\
 & + 1.957 \cdot 10^{-9}RS^3 \cdot TS^2
 \end{aligned} \tag{8}$$

$$\begin{aligned}
 PPA_{sB} = & -8.910 \cdot 10^2 + 3.336RS + 2.166 \cdot 10^2 TS - 4.083 \cdot 10^{-3} RS^2 \\
 & - 1.040 \cdot 10^1 TS^2 - 8.212 \cdot 10^{-1} RS \cdot TS + 1.621 \cdot 10^{-6} RS^3 \\
 & + 1.041 \cdot 10^{-3} RS^2 \cdot TS + 4.090 \cdot 10^{-2} RS \cdot TS^2 \\
 & - 4.285 \cdot 10^{-7} RS^3 \cdot TS - 5.425 \cdot 10^{-5} RS^2 \cdot TS^2 \\
 & + 2.328 \cdot 10^{-8} RS^3 \cdot TS^2
 \end{aligned}
 \tag{9}$$

$$\begin{aligned}
 PPB_{sB} = & -7.510 \cdot 10^2 + 2.502RS + 2.288 \cdot 10^2 TS - 2.680 \cdot 10^{-3} RS^2 \\
 & - 1.646 \cdot 10^1 TS^2 - 7.788 \cdot 10^{-1} RS \cdot TS + 9.353 \cdot 10^{-7} RS^3 \\
 & + 8.706 \cdot 10^{-4} RS^2 \cdot TS + 5.665 \cdot 10^{-2} RS \cdot TS^2 \\
 & - 3.167 \cdot 10^{-7} RS^3 \cdot TS - 6.372 \cdot 10^{-5} RS^2 \cdot TS^2 \\
 & + 2.328 \cdot 10^{-8} RS^3 \cdot TS^2
 \end{aligned}
 \tag{10}$$

$$\begin{aligned}
 PPC_{sB} = & -5.340 \cdot 10^2 + 2.136RS + 1.718 \cdot 10^2 TS - 2.626 \cdot 10^{-3} RS^2 \\
 & - 1.485 \cdot 10^1 TS^2 - 6.569 \cdot 10^{-1} RS \cdot TS + 1.036 \cdot 10^{-6} RS^3 \\
 & + 7.880 \cdot 10^{-4} RS^2 \cdot TS + 5.441 \cdot 10^{-2} RS \cdot TS^2 \\
 & - 3.038 \cdot 10^{-7} RS^3 \cdot TS - 6.264 \cdot 10^{-5} RS^2 \cdot TS^2 \\
 & + 2.328 \cdot 10^{-8} RS^3 \cdot TS^2
 \end{aligned}
 \tag{11}$$

$$\begin{aligned}
 PPD_{sB} = & -4.590 \cdot 10^2 + 1.781RS \\
 & + 1.676 \cdot 10^2 TS - 2.186 \cdot 10^{-3} RS^2 \\
 & - 1.194 \cdot 10^1 TS^2 \\
 & - 6.457 \cdot 10^{-1} RS \cdot TS + 8.645 \cdot 10^{-7} RS^3 \\
 & + 8.043 \cdot 10^{-4} RS^2 \cdot TS \\
 & + 4.612 \cdot 10^{-2} RS \cdot TS^2 \\
 & - 3.219 \cdot 10^{-7} RS^3 \cdot TS - 5.773 \cdot 10^{-5} RS^2 \cdot TS^2 \\
 & + 2.328 \cdot 10^{-8} RS^3 \cdot TS^2
 \end{aligned}
 \tag{12}$$

Figure 13a depicts in a Pareto chart, the statistical importance of the RS and TS coefficients regarding the tensile strength. All the terms were found to be statistically significant at a 0.05 level in the existing model, with the bars crossing the 1.98 margin. Figure 13b presents the residuals for each experimental repetition, while Fig. 13c presents the predicted with the model vs the corresponding experimental values for the tensile strength, for all the experimental measurements. The Mean Absolute Percentage Error (MAPE) was found to be 6.04%, which is an acceptable result. The Durbin-Watson factor (a measurement indicator

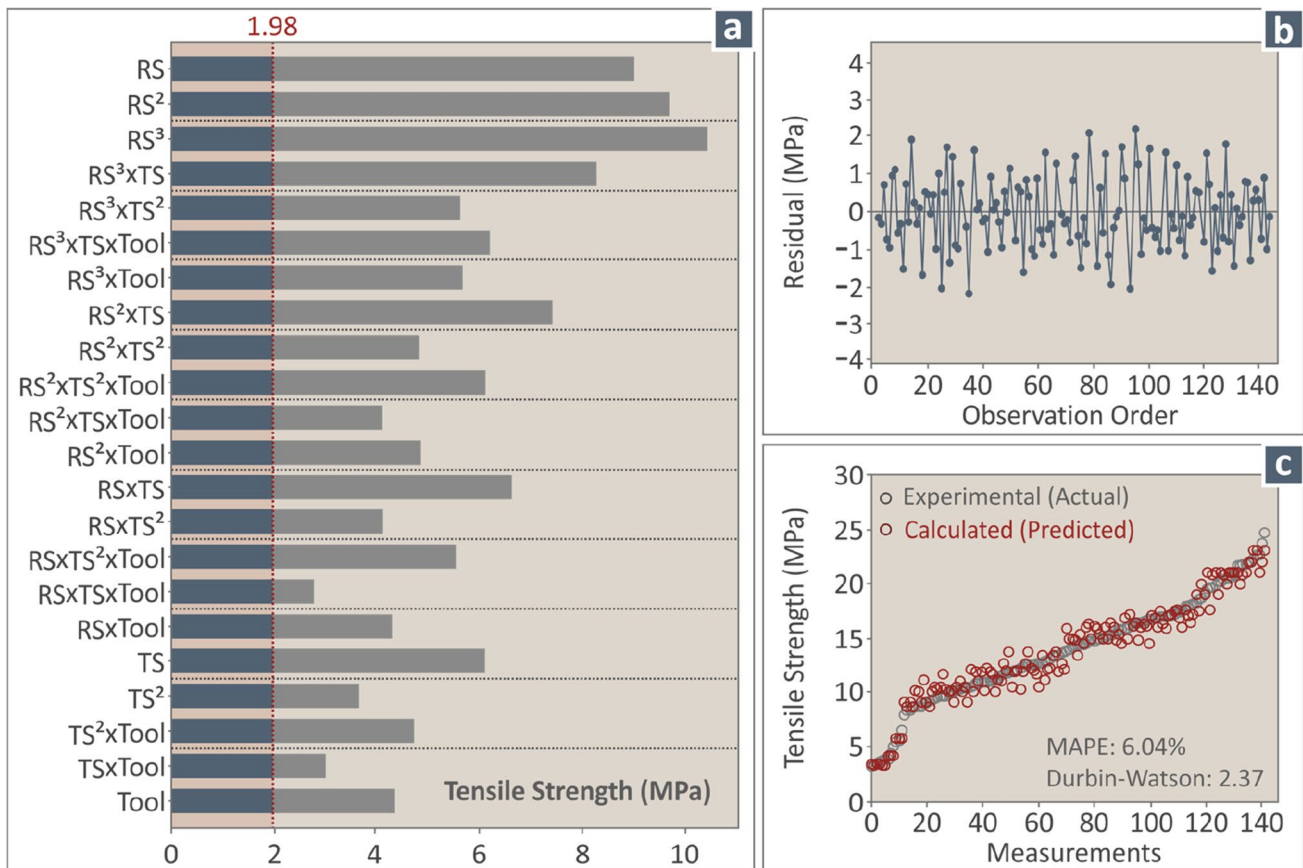


Fig. 13 (a) Pareto chart for the tensile strength vs the control parameters, (b) residuals for each repetition, and (c) experimental vs. calculated (predicted) graph, for all the measurements conducted in the work

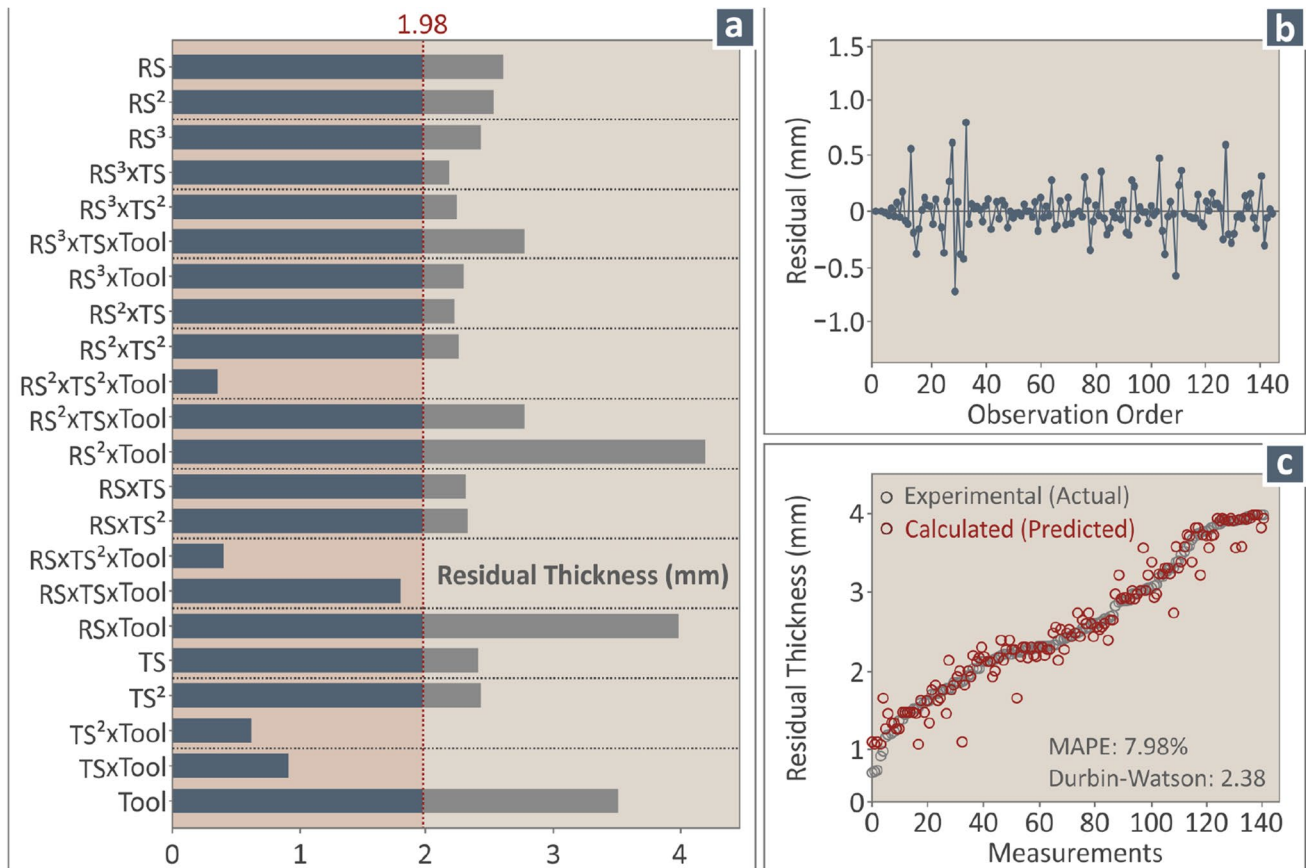


Fig. 14 (a) Pareto chart for the residual thickness vs. the control parameters, (b) residuals for each repetition, and (c) experimental vs. calculated (predicted) graph, for all the measurements conducted in the work

of the autocorrelation in the residuals) is 2.37 ($> 2, < 3$), showing a negligible and tolerable positive autocorrelation of the prediction residuals. Figure 14a depicts in a Pareto chart, the statistical importance of the RS and TS coefficients regarding the Residual Thickness response parameter. All the terms, except the $RS \times TS^2 \times Tool$, $RS^2 \times TS^2 \times Tool$, $RS \times TS \times Tool$, $TS^2 \times Tool$, and the $TS \times Tool$, were found to be statistically significant at a 0.05 level in the existing model, with the bars crossing the 1.98 margin. Figure 14b presents the residuals for each experimental repetition, while Fig. 14c presents the predicted with the model vs. the corresponding experimental values for the Residual Thickness, for all the experimental measurements. The Mean Absolute Percentage Error (MAPE) was found to be 7.98%, which is an acceptable result. The Durbin-Watson factor (a measurement indicator of the autocorrelation in the residuals), is 2.38 ($> 2, < 3$), showing a negligible and tolerable positive autocorrelation of the prediction residuals.

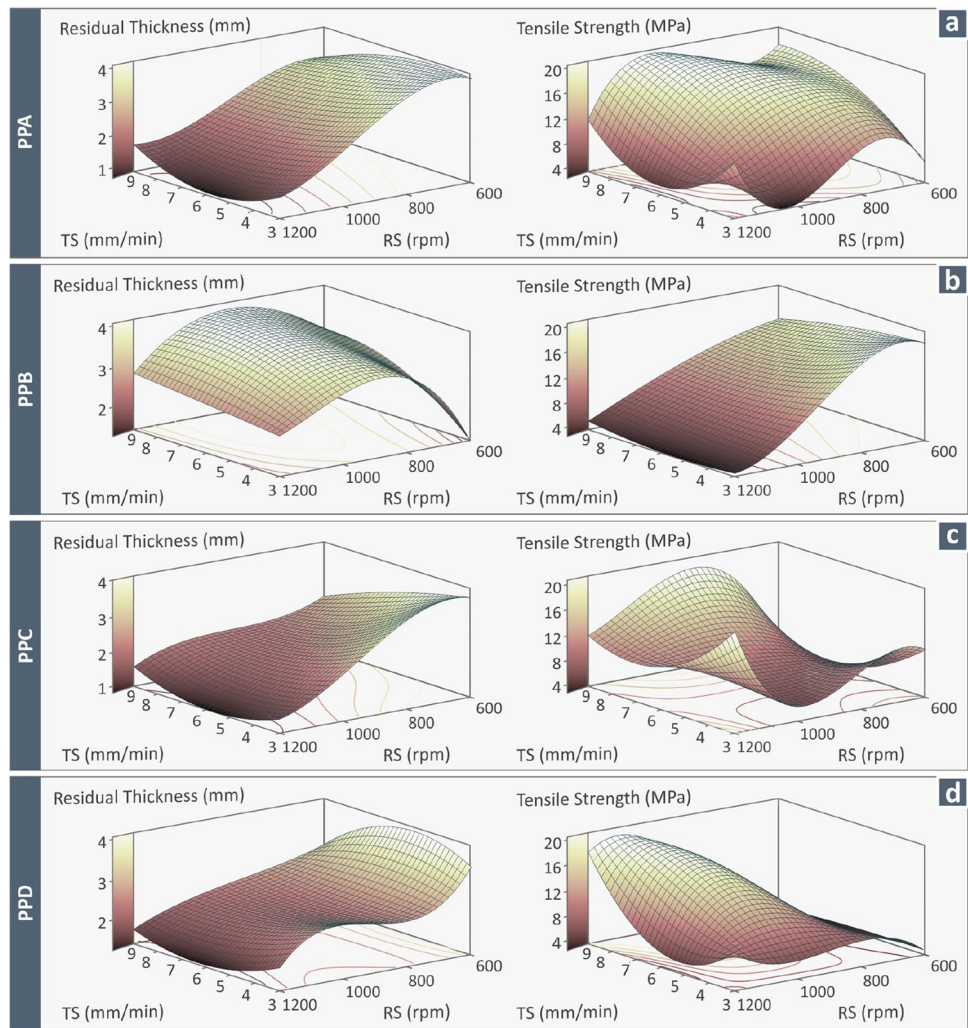
Please see the supplementary material of the work (Section A2 of the Appendix), for the corresponding ANOVA along with the Pareto charts of the Welding Temperature, the Tensile Modulus of Elasticity, and the Tensile Toughness

vs the control parameters studied. Figure 15 presents experimental data of the work (Residual Thickness – mm and tensile strength – MPa) as surface graphs compared to the four different welding tools developed and studied in the work.

4 Discussion

This work investigates the effect of three parameters affecting the performance of parts joined with the FSW process, i.e., RS (four levels), TS (three levels), and weld tool pin geometry (four levels). 3D printed PA6 of 4 mm thickness, were welded with the various parameters' values and the effect of the control parameters on the Residual Thickness of the weld of the joined parts, the welding temperature, and the tensile strength of the parts was investigated. The experimental results were analyzed and optimized with statistical modeling tools. No similar research is yet available in the literature for this material, the geometry of the samples, control parameters range values, and more importantly on 3D printed parts, for the evaluation of the effect of the 3D printing structure on the feasibility and

Fig. 15 Surface graphs of the residual thickness (mm) and the tensile strength (MPa) processing parameters vs. the welding tools studied: (a) PPA, (b) PPB, (c) PPC, (d) PPD



the performance of the FSW process. Still, the results of this study can be correlated with works in the literature, which are presented and analyzed in the introduction section of the work and investigate common scientific areas with the current work. In the work of Nandhini et al. [61] who studied FSW PA66 joints (bulk, not 3D printed), an 78% weld efficiency was achieved, and why in the current study a much higher weld efficiency of 120.04% was achieved. Also, in this work, the authors did not use statistical modeling tools to analyze the results, still they are reporting RS as the dominant parameter for the process. This partially agrees with the results of the current work, with RS being the rank 1 parameter for the tensile modulus and the Residual Thickness and the rank 2 parameter for the tensile strength. In another work on the effect of the FSW parameters in bulk PA66 sheets, [60], a 46% weld efficiency was achieved. The authors complied with an L9 orthogonal array with three control parameters (RS, TS, and plunge depth) with three levels each. The studied control parameters values are in a higher range than the

current work, but overall, the values are close. The RS was the dominant parameter in the process. Median RS values (1200 rpm) and low TS (10 mm/min) achieved the highest performance in the work. When studying thick (16 mm) bulk PA6 plates in FSW [63], it was found that temperature was a significant parameter affecting the tensile strength of the sample. This is not in good agreement with the findings of the current work, since the geometry of the welding tool only significantly affected the WT. It is also reported as the RS increases, joining PA6 plates is not possible and only lower RS values could achieve the welding of the plates. Such differences can be attributed to the different range of the FSW parameter values and most importantly, to the significantly different thickness of the plates studied, in which, as the authors mention, low melt viscosity response affects the process. When studying the effect of RS (five levels) and TS (three levels) on the mechanical performance of bulk PA66 sheets joined with FSW, it was found that the increase of RS, increases the mechanical performance for values up to 1570 rpm,

while further increase of the RS decreases the mechanical performance of the samples [59]. This effect was observed in the work presented herein for RS up to 1000 rpm. Further increase of the RS led to the decrease of the tensile strength, although the tensile modulus was further increasing up to the maximum RS of 1200 rpm studied. Differences can be attributed to different conditions, different PA grade and more importantly on the 3D printing structure of the samples studied in the current work. Regarding the TS, it is reported in the work of Husain et al. that the increase of TS negatively affects the mechanical performance, which is not in agreement with the findings of the current work, in which, the increase of TS, increased the tensile strength. TS values were in a different range in the two works.

The authors studied three FSW parameters, i.e., RS, TS, and weld tool pin geometry, with 3 levels each. The values range is not similar to that of the current work. Statistical modeling was employed to analyze and optimize the parameters. The median values of this work regarding the TS RS and the TS (1200 rpm, 40 mm/min) and high weld tool pin diameter (9 mm) achieved better mechanical properties in the welded samples. The weld efficiency achieved was 56.45% for the ABS and 13.91% for the PA6, which is much lower than the current work findings. This can be attributed to the difficulties the authors faced, owing to the different polymers welded.

Comparing the current work with similar works investigating the effects of the FSW parameters on the weld performance of 3D printed parts from other polymers, as expected some of the findings agree, while others are not in agreement. When correlating the results of the current work with a corresponding work on the PMMA polymer [56], the results agree regarding the TS (9 mm/min optimized the mechanical properties), agree regarding the significance of the WT, partially agree with the RS (1000 rpm in the current work, 1400 rpm for the PMMA polymer), and partially agree regarding the significance of the welding tool in achieving higher mechanical properties. Compared with the corresponding work for the ABS polymer [54], similar findings are reported regarding the weld tool and the RS, but the results differ regarding the TS, which was not a critical parameter affecting the strength of the joined samples, unlike the current work results, in which the increase of the TS constantly increased the tensile strength of the samples. When correlating the results with findings for the PLA polymer [55], the results of the work agree regarding the TS and the RS but are not in agreement regarding the effect of the weld tool geometry.

Regarding the developed temperatures in the polymer during the process, the TGA and DSC results show the welding process is safe. The Main Effect Plots indicate which parameters affect the temperature the most. For

example, in the PPD tool, the welding temperature was lower than in the other welding tools. This does not mean that the weld performance is better with this tool, so this should be considered as well and parameters should be set according to the required specifications in each case. Additionally, the equations provided in the supplementary material of the work for the calculation of the welding temperature, as a function of the control parameters, can be exploited for the evaluation of the welding temperature during the process, as they were proven reliable, by the confirmation tests conducted. Finally, the process for monitoring the welding temperature in the experiments is compatible with the literature [74].

5 Conclusions

This study proved that joining MEX 3D printing PA6 sheets with FSW is possible. Different FSW parameters (weld tool pin geometry, TS, RS) were studied for their effect on the mechanical strength of the welded parts in tensile tests. Results were analyzed with statistical tools, to evaluate the significance of each parameter and optimize the process.

- Four different weld tools were studied, one with a cylindrical pin, one with a frustum pin, and two more with the same geometry, but with threads on the pin.
- The mechanical strength of the samples was highly affected by the weld tool pin geometry.
- The TS was also an important parameter, with samples welded with high TS achieving better results in the tensile tests.
- The highest temperature was recorded with the frustum weld tool and the lowest with the threaded frustum weld tool.
- The highest tensile strength is reported at the sample welded with the PPC tool, at 800 rpm, which also achieved the highest tensile modulus of elasticity.
- The lower mechanical strength was reported on a sample welded with the threaded frustum weld tool.

The equations provided can be directly applied to industrial environments for the calculation of the response parameters and users can achieve higher values in specific response parameters, and anticipate the performance of the weld, in the remaining parameters. In future work, additional parameters and parameter values will be investigated, as the results indicate high sensitivity of the weld performance (mechanical strength results) when changing the parameter values. In future work, the authors intend to apply machine learning approaches to model the process between input and output parameters.

Supplementary Information The online version contains supplementary material available at <https://doi.org/10.1007/s00170-022-10675-5>.

Acknowledgements The authors would like to thank Aleka Manousaki from the Institute of Electronic Structure and Laser of the Foundation for Research and Technology, Hellas (IESL-FORTH), for taking the SEM images presented in this work.

Author contribution Nectarios Vidakis: Conceptualization, methodology, resources, supervision, project administration, writing—review, and editing; Markos Petousis: Methodology, formal analysis, writing—original draft preparation, writing—review, and editing; Nikolaos Mountakis: Software, formal analysis, investigation, data curation; J.D. Kechagias: formal analysis, data curation; The manuscript was written through contributions of all authors. All authors have approved the final version of the manuscript.

Data availability The raw/processed data required to reproduce these findings cannot be shared at this time due to technical or time limitations.

Declarations

Journal policies have been reviewed and accepted by all authors.

Competing interests The authors declare no competing interests.

Disclaimer The funding sponsors had no role in the design of the study; in the collection, analysis, or interpretation of data; in the writing of the manuscript, and in the decision to publish the results.

References

- Arhant M, Briançon C, Burtin C, Davies P (2019) Carbon/polyamide 6 thermoplastic composite cylinders for deep sea applications. *Compos Struct* 212:535–546. <https://doi.org/10.1016/j.compstruct.2019.01.058>
- Jimenez M, Gallou H, Duquesne S, Jama C, Serge Bourbigot XC, FS, (2012) New routes to flame retard polyamide 6, 6 for electrical applications. *J Fire Sci* 30:535–551. <https://doi.org/10.1177/0734904112449992>
- Goitisoló I, Eguiazábal JI, Nazábal J (2008) Effects of reprocessing on the structure and properties of polyamide 6 nanocomposites. *Polym Degrad Stab* 93:1747–1752. <https://doi.org/10.1016/j.polymdegradstab.2008.07.030>
- Su KH, Lin JH, Lin CC (2007) Influence of reprocessing on the mechanical properties and structure of polyamide 6. *J Mater Process Technol* 192–193:532–538. <https://doi.org/10.1016/j.jmatprotec.2007.04.056>
- Kumar SS, Kanagaraj G (2016) Evaluation of mechanical properties and characterization of silicon carbide–reinforced polyamide 6 polymer composites and their engineering applications. *Int J Polym Anal Charact* 21:378–386. <https://doi.org/10.1080/1023666X.2016.1160671>
- Karsli NG, Aytac A (2013) Tensile and thermomechanical properties of short carbon fiber reinforced polyamide 6 composites. *Compos Part B Eng* 51:270–275. <https://doi.org/10.1016/j.compositesb.2013.03.023>
- Luna CBB, Ferreira E da SB, Siqueira DD et al (2022) Electrical nanocomposites of PA6 ABS ABS-MA reinforced with carbon nanotubes MWCNTf. *Polym Compos* 1–20. <https://doi.org/10.1002/pc.26643>
- Meincke O, Kaempfer D, Weickmann H et al (2004) Mechanical properties and electrical conductivity of carbon-nanotube filled polyamide-6 and its blends with acrylonitrile/butadiene/styrene. *Polymer (Guildf)* 45:739–748. <https://doi.org/10.1016/j.polymer.2003.12.013>
- Jia Y, He H, Peng X, Meng S, Jian Chen YG (2017) Preparation of a new filament based on polyamide-6 for three-dimensional printing. *Polym Eng Sci*. <https://doi.org/10.1002/pen.24515>
- Vidakis N, Petousis M, Kechagias JD (2022) Parameter effects and process modelling of Polyamide 12 3D-printed parts strength and toughness. *Mater Manuf Process* 00:1–12. <https://doi.org/10.1080/10426914.2022.2030871>
- Vidakis N, Petousis M, Velidakis E et al (2020) On the strain rate sensitivity of fused filament fabrication (Fff) processed pla, abs, petg, pa6, and pp thermoplastic polymers. *Polymers (Basel)* 12:1–15. <https://doi.org/10.3390/polym12122924>
- Vidakis N, Petousis M, Tzounis L et al (2021) Sustainable additive manufacturing: mechanical response of polyamide 12 over multiple recycling processes. *Materials (Basel)* 14:1–15. <https://doi.org/10.3390/ma14020466>
- Bai J, Song J, Wei J (2019) Tribological and mechanical properties of MoS₂ enhanced polyamide 12 for selective laser sintering. *J Mater Process Technol* 264:382–388. <https://doi.org/10.1016/j.jmatprotec.2018.09.026>
- Cai C, Tey WS, Chen J et al (2021) Comparative study on 3D printing of polyamide 12 by selective laser sintering and multi jet fusion. *J Mater Process Technol* 288:116882. <https://doi.org/10.1016/j.jmatprotec.2020.116882>
- Threadgill PL, Leonard AJ, Shercliff HR, Withers PJ (2009) Friction stir welding of aluminium alloys. *Int Mater Rev* 54:49–93. <https://doi.org/10.1179/174328009X411136>
- Chien CH, Lin WB, Chen T (2011) Optimal FSW process parameters for aluminum alloys AA5083. *J Chinese Inst Eng Trans Chinese Inst Eng A* 34:99–105. <https://doi.org/10.1080/02533839.2011.553024>
- Vidakis N, Vairis A, Diouf D et al (2016) Effect of the tool rotational speed on the mechanical properties of thin AA1050 friction stir welded sheets. *J Eng Sci Technol Rev* 9:3
- Heinz B, Skrotzki B (2002) Characterization of a friction-stir-welded aluminum alloy 6013. *Metall Mater Trans B Process Metall Mater Process Sci* 33:489–498. <https://doi.org/10.1007/s11663-002-0059-5>
- Sakthivel T, Sengar GS, Mukhopadhyay J (2009) Effect of welding speed on microstructure and mechanical properties of friction-stir-welded aluminum. *Int J Adv Manuf Technol* 43:468–473. <https://doi.org/10.1007/s00170-008-1272-7>
- Fujii H, Cui L, Maeda M, Nogi K (2006) Effect of tool shape on mechanical properties and microstructure of friction stir welded aluminum alloys. *Mater Sci Eng A* 419:25–31. <https://doi.org/10.1016/j.msea.2005.11.045>
- Dimopoulos A, Vairis A, Vidakis N, Petousis M (2021) On the friction stir welding of al 7075 thin sheets. *Metals (Basel)* 11:1–12. <https://doi.org/10.3390/met11010057>
- Mironov S, Inagaki K, Sato YS, Kokawa H (2015) Effect of welding temperature on microstructure of friction-stir welded aluminum alloy 1050. *Metall Mater Trans A Phys Metall Mater Sci* 46:783–790. <https://doi.org/10.1007/s11661-014-2651-0>
- Li H, Gao J, Li Q (2018) Fatigue of friction stir welded aluminum alloy joints: a review. *Appl Sci* 8. <https://doi.org/10.3390/app8122626>
- Ghangas G, Singhal S, Dixit S et al (2022) Mathematical modeling and optimization of friction stir welding process parameters for armor-grade aluminium alloy. *Int J Interact Des Manuf*. <https://doi.org/10.1007/s12008-022-01000-1>
- Zamrudi FH, Setiawan AR (2022) Effect of friction stir welding parameters on corrosion behaviour of aluminium alloys: an overview. *Corros Eng Sci Technol* 1–12. <https://doi.org/10.1080/1478422X.2022.2116185>

26. Antoniadis A, Vidakis N, Bilalis N (2002) Fatigue fracture investigation of cemented carbide tools in gear hobbing, Part 2: the effect of cutting parameters on the level of tool stresses - a quantitative parametric analysis. *J Manuf Sci Eng* 124:792–798. <https://doi.org/10.1115/1.1511173>
27. Balamurugan S, Jayakumar K, Anbarasan B, Rajesh M (2022) Effect of tool pin shapes on microstructure and mechanical behaviour of friction stir welding of dissimilar aluminium alloys. *Mater Today Proc*. <https://doi.org/10.1016/j.matpr.2022.08.459>
28. Kubit A, Trzepieciński T, Kluz R et al (2022) Multi-criteria optimisation of friction stir welding parameters for EN AW-2024-T3 aluminium alloy joints. *Materials (Basel)* 15. <https://doi.org/10.3390/ma15155428>
29. Varunraj S, Ruban M (2022) Investigation of the microstructure and mechanical properties of AA6063 and AA7075 dissimilar aluminium alloys by friction stir welding process. *Mater Today Proc*. <https://doi.org/10.1016/j.matpr.2022.08.095>
30. Bagheri B, Sharifi F, Abbasi M, Abdollahzadeh A (2021) On the role of input welding parameters on the microstructure and mechanical properties of Al6061-T6 alloy during the friction stir welding: experimental and numerical investigation. *Proc Inst Mech Eng Part L J Mater Des Appl* 236:299–318. <https://doi.org/10.1177/14644207211044407>
31. Abdollahzadeh A, Bagheri B, Abbasi M et al (2021) Comparison of the weldability of AA6061-T6 joint under different friction stir welding conditions. *J Mater Eng Perform* 30:1110–1127. <https://doi.org/10.1007/s11665-020-05379-4>
32. Bagheri B, Abbasi M, Abdollahzadeh A, Kokabi AH (2020) Numerical analysis of cooling and joining speed effects on friction stir welding by smoothed particle hydrodynamics (SPH). *Arch Appl Mech* 90:2275–2296. <https://doi.org/10.1007/s00419-020-01720-4>
33. Bagheri B, Abdollahzadeh A, Abbasi M, Kokabi AH (2020) Numerical analysis of cooling and joining speed effects on friction stir welding by smoothed particle hydrodynamics (SPH). *Int J Adv Manuf Technol* 110:209–228. <https://doi.org/10.1007/s00170-020-05839-0>
34. Bagheri B, Abbasi M, Dadaei M (2020) Mechanical behavior and microstructure of AA6061-T6 joints made by friction stir vibration welding. *J Mater Eng Perform* 29:1165–1175. <https://doi.org/10.1007/s11665-020-04639-7>
35. Abbasi M, Bagheri B, Abdollahzadeh A, Moghaddam AO (2021) A different attempt to improve the formability of aluminum tailor welded blanks (TWB) produced by the FSW. *Int J Mater Form* 14:1189–1208. <https://doi.org/10.1007/s12289-021-01632-w>
36. Abbasi M, Abdollahzadeh A, Bagheri B et al (2021) Study on the effect of the welding environment on the dynamic recrystallization phenomenon and residual stresses during the friction stir welding process of aluminum alloy. *Proc Inst Mech Eng Part L J Mater Des Appl* 235:1809–1826. <https://doi.org/10.1177/14644207211025113>
37. Abdollahzadeh A, Bagheri B, Abbasi M et al (2021) A modified version of friction stir welding process of aluminum alloys: analyzing the thermal treatment and wear behavior. *Proc Inst Mech Eng Part L J Mater Des Appl* 235:2291–2309. <https://doi.org/10.1177/14644207211023987>
38. S S, Natarajan E, Shanmugam R, et al (2022) Strategized friction stir welded AA6061-T6/SiC composite lap joint suitable for sheet metal applications. *J Mater Res Technol* 21:30–39. <https://doi.org/10.1016/j.jmrt.2022.09.022>
39. Suresh S, Venkatesan K, Natarajan E, Rajesh S (2021) Performance analysis of nano silicon carbide reinforced swept friction stir spot weld joint in AA6061-T6 alloy. *SILICON* 13:3399–3412. <https://doi.org/10.1007/s12633-020-00751-4>
40. Suresh S, Venkatesan K, Natarajan E (2018) Influence of SiC nanoparticle reinforcement on FSS welded 6061-T6 aluminum alloy. *J Nanomater* 2018. <https://doi.org/10.1155/2018/7031867>
41. Kallee SW (2009) Industrial applications of friction stir welding. Woodhead Publishing Limited, 118–163. <https://doi.org/10.1533/9781845697716.1.118>
42. Bhardwaj N, Narayanan RG, Dixit US, Hashmi MSJ (2019) Recent developments in friction stir welding and resulting industrial practices. *Adv Mater Process Technol* 5:461–496. <https://doi.org/10.1080/2374068X.2019.1631065>
43. Kumar R, Singh R, Ahuja IPS et al (2018) Weldability of thermoplastic materials for friction stir welding- a state of art review and future applications. *Compos Part B Eng* 137:1–15. <https://doi.org/10.1016/j.compositesb.2017.10.039>
44. Gao J, Cui X, Liu C, Shen Y (2017) Application and exploration of friction stir welding/processing in plastics industry. *Mater Sci Technol (United Kingdom)* 33:1145–1158. <https://doi.org/10.1080/02670836.2016.1276251>
45. Elyasi M, Derazkola HA (2018) Experimental and thermo-mechanical study on FSW of PMMA polymer T-joint. *Int J Adv Manuf Technol* 97:1445–1456. <https://doi.org/10.1007/s00170-018-1847-7>
46. Banjare PN, Sahlot P, Arora A (2017) An assisted heating tool design for FSW of thermoplastics. *J Mater Process Technol* 239:83–91. <https://doi.org/10.1016/j.jmatprotec.2016.07.035>
47. Singh S, Prakash C, Gupta MK (2020) On friction-stir welding of 3D printed thermoplastics. 75–91. https://doi.org/10.1007/978-3-030-18854-2_3
48. Kumar R, Ranjan N, Kumar V et al (2022) Characterization of friction stir-welded polylactic acid/aluminum composite primed through fused filament fabrication. *J Mater Eng Perform* 31:2391–2409. <https://doi.org/10.1007/s11665-021-06329-4>
49. Sheikh-Ahmad JY, Ali DS, Deveci S et al (2019) Friction stir welding of high density polyethylene—carbon black composite. *J Mater Process Technol* 264:402–413. <https://doi.org/10.1016/j.jmatprotec.2018.09.033>
50. Lambiase F, Paoletti A, Grossi V, Di Ilio A (2019) Analysis of loads, temperatures and welds morphology in FSW of polycarbonate. *J Mater Process Technol* 266:639–650. <https://doi.org/10.1016/j.jmatprotec.2018.11.043>
51. Tiwary VK, Padmakumar A, Malik VR (2022) Investigations on FSW of nylon micro-particle enhanced 3D printed parts applied to a Clark-Y UAV wing. *Weld Int* 0:1–15. <https://doi.org/10.1080/09507116.2022.2104141>
52. Kumar R, Singh R, Ahuja IS (2020) Friction stir welding of three-dimensional printed polymer composites with semi-consumable tool. *Advances in additive manufacturing and joining*. Springer Singapore. https://doi.org/10.1007/978-981-32-9433-2_2
53. Kechagias JD, Ninikas K, Petousis M et al (2021) An investigation of surface quality characteristics of 3D printed PLA plates cut by CO2 laser using experimental design. *Mater Manuf Process* 36:1544–1553. <https://doi.org/10.1080/10426914.2021.1906892>
54. Vidakis N, Petousis M, Korlos A et al (2022) Friction stir welding optimization of 3D-printed acrylonitrile butadiene styrene in hybrid additive manufacturing. *Polymers (Basel)* 14:2474. <https://doi.org/10.3390/polym14122474>
55. Vidakis N, Petousis M, Mountakis N, Kechagias JD (2022) Material extrusion 3D printing and friction stir welding : an insight into the weldability of polylactic acid plates based on a full factorial design. *Int J Adv Manuf Technol*. <https://doi.org/10.1007/s00170-022-09595-1>
56. Vidakis N, Petousis M, Mountakis N, Kechagias JD (2022) Optimization of friction stir welding parameters in hybrid additive manufacturing: weldability of 3D-printed poly(methyl methacrylate) plates. *J Manuf Mater Process* 6:4. <https://doi.org/10.3390/jmmp6040077>

57. Kumar R, Singh R, Ahuja IPS, Fortunato A (2020) Thermo-mechanical investigations for the joining of thermoplastic composite structures via friction stir spot welding. *Compos Struct* 253:112772. <https://doi.org/10.1016/j.compstruct.2020.112772>
58. Bagheri A, Aghareb Parast MS, Kami A et al (2022) Fatigue testing on rotary friction-welded joints between solid ABS and 3D-printed PLA and ABS. *Eur J Mech - A/Solids* 96:104713. <https://doi.org/10.1016/j.euromechsol.2022.104713>
59. Husain IM, Salim RK, Azdast T, et al (2015) Mechanical properties of friction-stir-welded polyamide sheets. *Int J Mech Mater Eng* 10. <https://doi.org/10.1186/s40712-015-0047-6>
60. Nandhini R, Moorthy MK, Muthukumaran S (2017) Effect of welding parameters on microstructure and tensile strength of friction stir welded pa 6,6 joints. *Int Polym Process* 32:416–424. <https://doi.org/10.3139/217.3296>
61. Nandhini R, Dinesh Kumar R, Muthukumaran S, Kumaran S (2019) Optimization of welding process parameters in novel friction stir welding of polyamide 66 joints. *Mater Sci Forum MSF* 969:828–833. <https://doi.org/10.4028/www.scientific.net/MSF.969.828>
62. Nandhini R, Moorthy MK, Muthukumaran S, Kumaran S (2019) Influence of process variables on the characteristics of friction-stir-welded polyamide 6,6 joints. *Materwiss Werksttech* 50:1139–1148. <https://doi.org/10.1002/mawe.201800119>
63. Zafar A, Awang M, Khan SR, Emamian S (2016) Investigating friction stir welding on thick nylon 6 plates. *Weld J* 95:210s–218s
64. Zinati RF, Razfar MR (2015) Finite element simulation and experimental investigation of friction stir processing of Polyamide 6. *Proc Inst Mech Eng Part B J Eng Manuf* 229:2205–2215. <https://doi.org/10.1177/0954405414546705>
65. Farshbaf Zinati R, Razfar MR, Nazockdast H (2014) Numerical and experimental investigation of FSP of PA 6/MWCNT composite. *J Mater Process Technol* 214:2300–2315. <https://doi.org/10.1016/j.jmatprotec.2014.04.026>
66. Yan Y, Shen Y, Lei H et al (2020) Friction lap welding AA6061 alloy and GFR nylon: Influence of welding parameters and groove features on joint morphology and mechanical property. *J Mater Process Technol* 278:116458. <https://doi.org/10.1016/j.jmatprotec.2019.116458>
67. Kumar R, Singh R, Ahuja IPS (2019) Mechanical, thermal and micrographic investigations of friction stir welded: 3D printed melt flow compatible dissimilar thermoplastics. *J Manuf Process* 38:387–395. <https://doi.org/10.1016/j.jmapro.2019.01.043>
68. Singh R, Kumar R, Ahuja IPS (2021) Friction Welding for functional prototypes of PA6 and ABS with Al powder reinforcement. *Proc Natl Acad Sci India Sect A - Phys Sci* 91:351–359. <https://doi.org/10.1007/s40010-020-00659-z>
69. Tiwary VK, Ravi NJ, Arunkumar P et al (2020) Investigations on friction stir joining of 3D printed parts to overcome bed size limitation and enhance joint quality for unmanned aircraft systems. *Proc Inst Mech Eng Part C J Mech Eng Sci* 234:4857–4871. <https://doi.org/10.1177/0954406220930049>
70. Derazkola HA, Eyvazian A, Simchi A (2020) Modeling and experimental validation of material flow during FSW of polycarbonate. *Mater Today Commun* 22:100796. <https://doi.org/10.1016/j.mtcomm.2019.100796>
71. Vidakis N, Petousis M, Michailidis N et al (2022) Development and optimization of medical-grade multifunctional polyamide 12-cuprous oxide nanocomposites with superior mechanical and antibacterial properties for cost-effective 3D printing. *Nanomaterials* 12. <https://doi.org/10.3390/nano12030534>
72. Chakule RR, Chaudhari SS, Talmale PS (2021) Modelling and optimisation of nanocoolant minimum quantity lubrication process parameters for grinding performance. *Int J Exp Des Process Optim* 6:333–348. <https://doi.org/10.1504/IJEDPO.2021.123111>
73. Phadke MS (1995) *Quality engineering using robust design*, 1st edn. Prentice Hall PTR, USA
74. Sheikh-Ahmad JY, Deveci S, Almaskari F, Rehman RU (2022) Effect of process temperatures on material flow and weld quality in the friction stir welding of high density polyethylene. *J Mater Res Technol* 18:1692–1703. <https://doi.org/10.1016/j.jmrt.2022.03.082>

Publisher's note Springer Nature remains neutral with regard to jurisdictional claims in published maps and institutional affiliations.

Springer Nature or its licensor (e.g. a society or other partner) holds exclusive rights to this article under a publishing agreement with the author(s) or other rightsholder(s); author self-archiving of the accepted manuscript version of this article is solely governed by the terms of such publishing agreement and applicable law.